

Hydrodynamics of water-worked and screeded gravel beds: A comparative study

Ellora Padhi, Nadia Penna, Subhasish Dey, and Roberto Gaudio

Citation: *Physics of Fluids* **30**, 085105 (2018); doi: 10.1063/1.5044479

View online: <https://doi.org/10.1063/1.5044479>

View Table of Contents: <http://aip.scitation.org/toc/phf/30/8>

Published by the [American Institute of Physics](#)

Articles you may be interested in

[Review Article: Advances in modeling of bed particle entrainment sheared by turbulent flow](#)

Physics of Fluids **30**, 061301 (2018); 10.1063/1.5030458

[Referee Acknowledgment for 2017](#)

Physics of Fluids **30**, 010201 (2018); 10.1063/1.5022671

[Mixed ice accretion on aircraft wings](#)

Physics of Fluids **30**, 027101 (2018); 10.1063/1.5007301

[Exact solutions for oscillatory shear sweep behaviors of complex fluids from the Oldroyd 8-constant framework](#)

Physics of Fluids **30**, 030703 (2018); 10.1063/1.5023586

[A smoothed particle hydrodynamics \(SPH\) study on polydisperse sediment from technical activities on seabed](#)

Physics of Fluids **30**, 023302 (2018); 10.1063/1.5019811

[Hydrodynamic instability of meandering channels](#)

Physics of Fluids **29**, 125107 (2017); 10.1063/1.5012596

PHYSICS TODAY

WHITEPAPERS

ADVANCED LIGHT CURE ADHESIVES

Take a closer look at what these environmentally friendly adhesive systems can do

READ NOW

PRESENTED BY
 MASTERBOND
ADHESIVES | SEALANTS | COATINGS

Hydrodynamics of water-worked and screeded gravel beds: A comparative study

Ellora Padhi,^{1,a)} Nadia Penna,^{2,b)} Subhasish Dey,^{1,3,4,c)} and Roberto Gaudio^{2,d)}

¹Department of Civil Engineering, Indian Institute of Technology Kharagpur, Kharagpur, West Bengal 721302, India

²Dipartimento di Ingegneria Civile, Università della Calabria, 87036 Rende, Cosenza, Italy

³Physics and Applied Mathematics Unit, Indian Statistical Institute Kolkata, West Bengal 700108, India

⁴Department of Hydraulic Engineering, State Key Laboratory of Hydro-Science and Engineering, Tsinghua University, Beijing 100084, China

(Received 13 June 2018; accepted 31 July 2018; published online 21 August 2018)

The turbulence characteristics within flows over water-worked gravel beds (WGBs) and screeded gravel beds (SGBs) were examined by measuring the instantaneous flow velocity field using a two-dimensional particle image velocimetry system. To compare the responses of a WGB and an SGB to velocity and various turbulence characteristics, the flow Froude number was kept identical for both the beds that remained immobile. The roughness structures of both the beds were measured using a laser scanner. The results showed that the bed surface roughness was higher in the WGB than in the SGB. However, the longest axis of the gravels of WGBs was oriented streamwise owing to the action of water work, but the gravels of SGBs were randomly poised. The distribution of bed roughness fluctuations was negatively skewed in the WGB and positively skewed in the SGB. Double averaging methodology was applied to analyze the flow parameters. In this paper, the vertical profiles of the double-averaged streamwise velocity and the turbulence parameters, specifically the spatially averaged (SA) Reynolds shear and normal stresses, form-induced shear and normal stresses, turbulent kinetic energy (TKE) and form-induced TKE fluxes, quadrant analysis of SA Reynolds shear stress, etc., are presented and analyzed critically by focusing on comparisons between a WGB and an SGB. A comparative study reveals that in the near-bed flow zone, the SGB underestimates the turbulence parameters compared to the WGB. Therefore, in order to represent the prototypical flow in laboratory, the experiments should be performed in a WGB. *Published by AIP Publishing.* <https://doi.org/10.1063/1.5044479>

I. INTRODUCTION

Flow over a gravel bed, especially in the near-bed flow zone, has been of continued research interest for several decades owing to its practical importance.^{1–8} Gravel-bed flow is heavily influenced by colossal fluid–particle interactions, such as wake flow downstream of gravels, accelerated flow over gravel crests, and decelerated flow in interstices of gravels. These complex fluid–particle interactions give rise to spatial flow heterogeneities and are to enhance temporal intermittency in the near-bed flow.^{9–13} It is therefore important to understand the turbulent flow characteristics that arise from these complex turbulence mechanisms by resolving spatial flow heterogeneities. This enables us to accurately estimate the resistance to a hydraulically macro-rough flow (e.g., a mountainous river flow over a gravelly or a bouldery bed) and/or to predict the particle transport rate. In a natural river, the flow velocity plays a significant role in developing the bed surface topography formed by various roughness elements. Specifically, the gravels at the bed surface move if the flow velocity exceeds the threshold velocity for

gravel motion. Thus, the surface topography of a natural gravel bed exhibits spatially multifaceted, three-dimensional organization (orientation, alignment, spacing, and clustering of the gravel deposits) because it is created by transport processes as a result of continual deposition and reworking by several flood cycles. In this way, a so-called *water-worked gravel bed* (WGB) is formed in a natural river.

By contrast, laboratory experimental flume studies typically use a simulated gravelly riverbed that is prepared by randomly depositing mixed gravels into the flume to reach a given thickness. The gravel-bed surface is then scraped and leveled, forming a *screeded gravel bed* (SGB). The statistical distributions in terms of bed surface topography of an SGB are unable to appropriately represent a WGB, even though the bed surface formed by the gravels has the same particle size distribution. The WGB can however be generated in a laboratory flume transporting the gravel deposits by the flow. Notably the laboratory gravel bed can be deemed acceptable provided that the orientation, alignment, spacing, and clustering of gravels are analogous to the conditions in the prototype and that the distribution of the scaled gravel size is similar to that of the natural gravel bed. Importantly, the signature of bed roughness characteristic is effectively transmitted to the time-averaged flow characteristics, turbulence parameters, and resistance to flow.

Although extensive experimental studies on rough-bed flow have been performed, most have used SGBs. The SGB

^{a)}ellora@iitkgp.ac.in

^{b)}nadia.penna@unical.it

^{c)}sdey@iitkgp.ac.in

^{d)}Author to whom correspondence should be addressed: gaudio@unical.it

surface topographies are quite different from those of natural gravel riverbeds. Only a handful of researchers performed experimental studies on WGBs, which more closely resemble natural gravel beds. Cooper and Tait¹⁴ and Hardy *et al.*¹⁵ performed various experiments and concluded that the time-averaged flow over a WGB is spatially heterogeneous and strongly influenced by the relative submergence. Furthermore, Cooper and Tait¹⁶ performed experiments using both WGBs and SGBs to examine the spatial features of time-averaged streamwise velocity in the near-bed flow zone. They observed that the distribution of bed surface fluctuations was almost symmetric and positively skewed in a WGB, but negatively skewed in an SGB. Furthermore, the standard deviation of the bed surface fluctuations in a WGB was found to be higher than that in an SGB. The effects of the bed surface geometry and roughness were reflected by the differences between the flow characteristics over the WGB and SGB. Other researchers also studied turbulent flow characteristics over WGBs in order to explore the effects of bed roughness on the streamwise velocity, Reynolds shear stress (RSS), Reynolds normal stresses, and form-induced shear stress profiles.^{17–22} Despite these experimental studies, a detailed turbulence analysis that compares the higher order turbulence statistics [i.e., turbulent kinetic energy (TKE) flux and form-induced TKE flux], conditional RSS, and specific temporal flow pictures of WGBs and SGBs is not available.

Further in order to resolve the spatial flow heterogeneity, area averaging of the time-averaged quantities is performed over the layer parallel to the mean bed surface, called the *double-averaging methodology* (DAM).^{23–27} In DAM, the local time-averaged quantity $\bar{\theta}$ is decomposed as $\bar{\theta} = \langle \bar{\theta} \rangle + \tilde{\theta}$, where $\tilde{\theta}$ is the fluctuations in $\bar{\theta}$ with respect to the double-averaged (DA) quantity $\langle \bar{\theta} \rangle$. By Reynolds decomposition, an instantaneous quantity θ is given by $\theta = \bar{\theta} + \theta'$, where θ' is the fluctuations in θ with respect to $\bar{\theta}$. Here, the angle bracket $\langle - \rangle$ indicates the intrinsic spatial average. Below the crest of roughness elements, a roughness geometry function $\phi(z)$ ($= A_f/A_0$) that contributes to a superficial DA flow is introduced as a multiplier of the intrinsic DA flow quantity $\langle \bar{\theta} \rangle$.⁸ Here, $A_f(z)$ is the fluid-occupied area at an elevation z below the crest ($z < 0$, where z has an origin at the crest and is positive above the crest) and A_0 is the total area over which the average is calculated. The roughness layer is divided into two sublayers: the form-induced and interfacial sublayers (Fig. 1).

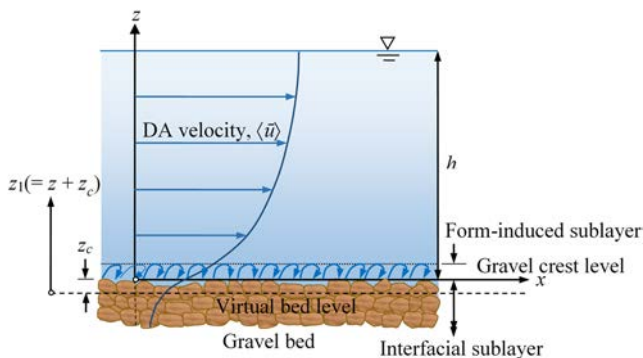


FIG. 1. Schematic of turbulent flow over a macro-rough bed with flow sublayers.

The form-induced sublayer is the flow region between the top of the roughness layer and the roughness crest, while the interfacial sublayer is the flow region below the crest. These sublayers are influenced by individual roughness elements.

The aim of this study was therefore to examine the spatially averaged (SA) turbulent flow characteristics over a WGB and an SGB prepared using the same gravel samples. This paper thus highlights how the bed surface topography of a WGB influences the turbulence characteristics in the near-bed flow zone differently from that of an SGB when the same gravels and flow conditions are used. It therefore provides improved descriptions of the differences between WGB and SGB turbulence characteristics such as the DA streamwise velocity, SA RSS, Reynolds normal stresses, TKE flux, RSS quadrant analysis, form-induced shear stress, form-induced normal stresses, etc. However, the flow characteristics were measured only in the vertical plane along the streamwise direction, because a two-dimensional particle image velocimetry (PIV) system was employed.

II. EXPERIMENTAL APPARATUS AND PROCEDURE

Experiments were performed in the *Grandi Modelli Idraulici* laboratory at the Università della Calabria, Italy. A 9.6 m long, 0.485 m wide, 0.5 m deep rectangular tilting flume was used. The inlet of the flume consisted of a stilling tank, an uphill slipway, and a honeycomb designed to dampen the flow disturbances. The flow depth in the flume was regulated by adjusting the downstream tailgate. A tank was attached downstream of the tailgate to collect the outflow. A gravel trap was placed over the tank to collect the transported gravel particles. The flow discharge in the flume was metered using a calibrated Thomson weir fitted at the outlet of the tank. The experimental bed was prepared using coarse gravels with a unimodal size distribution ($4 < d < 6$ mm) having a median size of $d_{50} = 4.81$ mm. The geometric standard deviation σ_g [$= (d_{84}/d_{16})^{0.5}$] of the gravel sample was 1.18 (< 1.4), which indicates that the gravel particles were uniform. The gravels were considerably non-spherical (approximately elliptical cross-section tapering toward each end), having the average longest, intermediate, and shortest axial lengths of individual gravels of $a = 12.3$ mm, $b = 5.9$ mm, and $c = 4.5$ mm, respectively. The flume walls were made of glass enabling us to visualize the flow. All measurements were taken within a 1 m long zone from 6.3 m to 7.3 m of the flume inlet. To ensure the fully developed flow, the flow development length was calculated from the boundary layer thickness formula²⁸ ($\delta = 0.33xu^*/U$, where x is the streamwise distance, u^* is the shear velocity, and U is the maximum flow velocity) and found to be 2.24 m from the inlet. In addition, the velocity profiles within the test section were found to be fully developed, which confirmed the fully developed flow in the test section. Furthermore, the uniformity of flow in the test section was ascertained by measuring the flow profile with a point gauge. During flow measurements for both the WGB and SGB, the flow depths were maintained same by regulating the adjustable downstream tailgate. Thus, the flow Froude numbers were identical. A schematic diagram of the experimental flume and instruments is shown in Fig. 2(a).

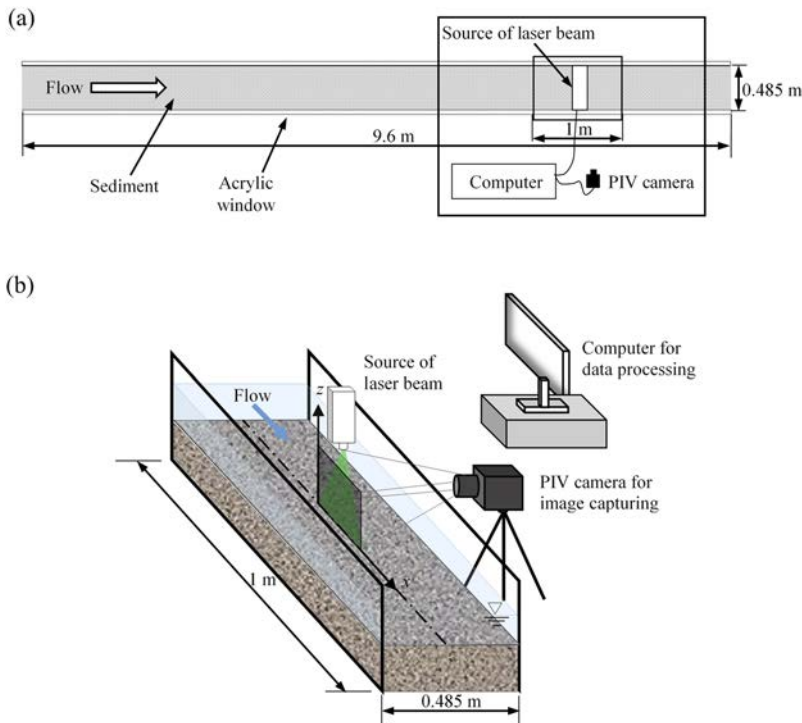


FIG. 2. Schematic of (a) the experimental apparatus (plan view) and (b) the flume test section showing the laser pulser and PIV camera (both connected to a synchronizer to aid in capturing frames produced during laser emission), as well as the computer used for data processing.

The flow field over the gravel bed was measured using a two-dimensional (2D) particle image velocimetry system manufactured by TSI [Fig. 2(b)]. It consisted of a Nikon 12 bit charge-coupled device (CCD) camera, model 630091 POWERVIEW Plus 4M, with 2048×2048 square pixels, and a frame rate of 15 Hz, as well as a double-pulse Nd:YAG laser, model EverGreen 200 manufactured by Quantel, with a pulse energy of 200 mJ at a wavelength of 532 nm. The laser pulser and the camera were synchronized by a LaserPulse Synchronizer Model 610036. Two (one spherical and one cylindrical) lenses were attached to the laser head nozzle to illuminate the flow with a light sheet having a thickness of 2 mm. Although the PIV system used in this study can work at 15 Hz, it was operated at 7.25 Hz owing to a PC port frequency limitation. Furthermore, the double-frame mode was used to achieve a satisfactory spatiotemporal resolution, where two images were captured within a very short time equaling $1000 \mu\text{s}$. This inter-frame time (time delay) between the two laser pulses should be long enough for determining the displacement of the seeding particles in the pair of images with sufficient resolution. On the other hand, inter-frame time should be short enough to avoid particles with an out-of-plane velocity component leaving the laser sheet between subsequent pulses. It means that the inter-frame time was fixed to optimize the particle image displacement between the two captured frames according to the flow velocity. It was set during preliminary tests for the regulation of the amount of seeding particles to be used during the experiments. To discuss further, it follows that in the space domain, considering a mean flow velocity of 0.43 m s^{-1} and the fixed inter-frame time, we were able to measure only eddies greater than 0.43 mm . However, the actual size of the eddy was imposed by the spatial resolution of the PIV measurements. Having known the inter-frame time and computed the displacement of a seeding particle, the instantaneous velocity of the particle was estimated.

The INSIGHT 4G-2DTR software was used to control data acquisition and to process the resulting data. Titanium dioxide particles with a mean size of $3 \mu\text{m}$ and a mass density of $4.26 \times 10^3 \text{ kg m}^{-3}$ were used as seeding particles and fed into the flow upstream. The seeding particles were fine enough to become ambient fluid particles even though their mass density was greater than that of water.^{29,30} Furthermore, care was taken to feed the seeding particles into the flow in a manner that satisfied the general criteria for an accurate PIV measurement.³¹ The laser sheet illuminated the test section in order to aid in visualizing the seeding particle motion captured by using the camera placed parallel to the laser sheet.^{19,32,33} The base of the PIV camera was aligned parallel to the average bed level having an elevation of lens centerline (cross-hair) 5 cm from the average bed level [Fig. 2(b)],¹⁹ enabling us to identify the flow below the crest with no excessive reflection of the laser light from the bed surface. However, in some locations along the laser sheet, the camera visual field was to some extent blocked by some gravels immediate across the laser sheet.

In this study, an interrogation area (IA) contained 64×64 square pixels, each with a size of about $2.7 \times 2.7 \text{ mm}^2$. Thus, the overall area of an image was $170 \times 170 \text{ mm}^2$. No overlapping IAs were considered, as they would have increased the computation time significantly without improving the results. During the experiments, the laser sheet along with the camera was shifted to each measuring location, and then the flow measurements were taken. Altogether 3000 pairs of images were captured on a vertical plane along the flume centerline in order to measure the flow field over a period of 414 s at each streamwise location, such as 0.06 m, 0.26 m, 0.46 m, 0.66 m, and 0.94 m from the starting point of the test section. This duration of the test significantly exceeded that recommended for measurements in boundary layer flow.^{34,35} The image particle size was less than 1 pixel. Thus, to minimize the effect of peak locking, first of all the images were

pre-processed by using a filter (already available in the INSIGHT 4G-2DTR software), which optimized the particle image diameter with respect to the peak estimator. This filter subtracted the background image of a seeding particle (that is the fixed part of the image itself) in order to make more apparent the moving seeding particles (that is the variable part) and to improve the signal to noise ratio. Then, the Gaussian interpolation was used in order to determine the correlation peaks and the average seeding particle displacement over an interrogation area with a sub-pixel accuracy. The image analysis provided 43 velocity profiles on a vertical plane in the streamwise direction, covering an area of $120 \times 100 \text{ mm}^2$ with a spatial resolution of 2.7 mm in both vertical and streamwise directions at each measuring location. No data cleaning process was used in analyzing the data.

In the first phase, gravel particles were placed in the flume and screeded manually to form the SGB and the bed surface fluctuations were measured using a laser scanner (Leica ScanStation P20), having an accuracy of $\pm 3 \text{ mm}$ at 50 m and $\pm 6 \text{ mm}$ at 100 m. The average bed slope was found to be 0.7%. Next, the WGB was generated by initiating flow over the SGB in a manner that could transport the surface gravels. The flow depth h used to prepare the WGB was 0.088 m, as measured from the gravel crest. The threshold flow velocity U_c needed to initiate bed-particle motion was determined via Neill's³⁶ empirical formula to be 0.59 m s^{-1} . This is less than the average flow velocity $U_{avg} [= Q/(Bh)$, where Q is the flow discharge and B is the flume width] of 0.82 m s^{-1} . The gravel transport rate (g_s) for the WGB preparation declined from $7.2 \times 10^{-2} \text{ kg m}^{-1} \text{ s}^{-1}$ to $3 \times 10^{-4} \text{ kg m}^{-1} \text{ s}^{-1}$ over a period of 28.5 h because no gravel was fed. The flow was stopped at the end of this phase. Then, the bed surface fluctuations were measured using the laser scanner, and the average bed slope was found to be 0.4%.

In the second phase, the flume was cleaned and the gravel particles were again placed in the flume and manually screeded to create a new SGB. The bed slope of the new SGB was identical to that of the earlier SGB ($= 0.7\%$) in order to understand the effects (before and after) of the water-work on the flow characteristics and bed topographies. By analyzing the bed surface fluctuations of the entire test section derived from the detrended laser scans of the bed topography, the crests of gravels having the highest elevation, considered to be the crest level, were obtained. Then, they were compared with the lower boundary of the flow field obtained from the PIV images.

From the bed surface fluctuations, the virtual bed levels (mean bed levels corresponding to $z = -z_c$ or $z_1 = 0$, where z_c is the crest level) were computed for the WGB and SGB (Fig. 1). The WGB and SGB gravel crest levels z_c ($z = 0$ or $z_1 = z_c$) were estimated to be 0.00196 m and 0.00283 m, respectively, above the virtual level. The average roughness heights Δ_k were approximately equal to the standard deviations of the bed surface fluctuations. They were found to be 1.25 mm and 1.04 mm for the WGB and SGB, respectively. These values can be interpreted as the characteristic roughness of the two different beds.^{37,38} The bed surface fluctuations measured along the WGB centerline that form the bed roughness follow an asymmetric distribution with a skewness of -0.93 and a kurtosis of 3.26 [Fig. 3(a)]. By contrast, the fluctuations along the SGB centerline follow an asymmetric distribution with a skewness of 0.04 and a kurtosis of 2.41 [Fig. 3(b)].

The autocorrelation function R_{lx} was calculated to determine the horizontal length scales λ_x for both the WGB and SGB (Fig. 4) as

$$R_{lx} = \frac{1}{N-n} \sum_{i=1}^{N-n} [z'(x_i)z'(x_i + n\delta x)], \quad (1)$$

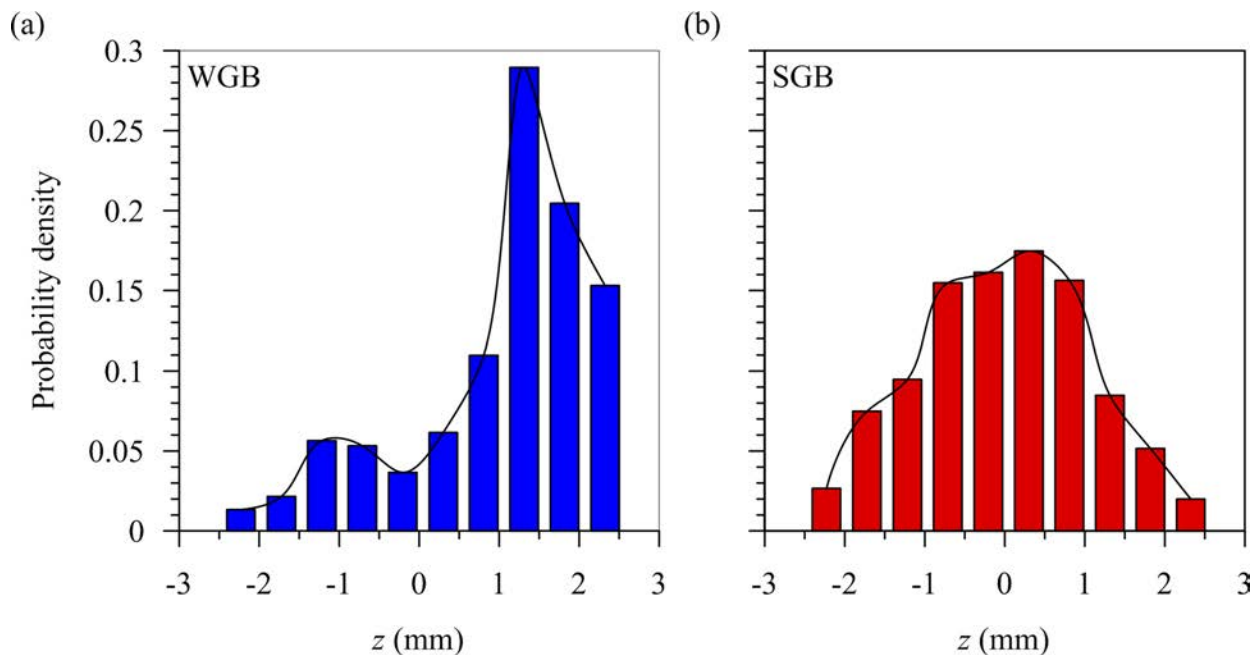


FIG. 3. The probability density functions and histograms of bed surface fluctuations as a function of mean surface elevation along the flume centerline in (a) the WGB and (b) the SGB.

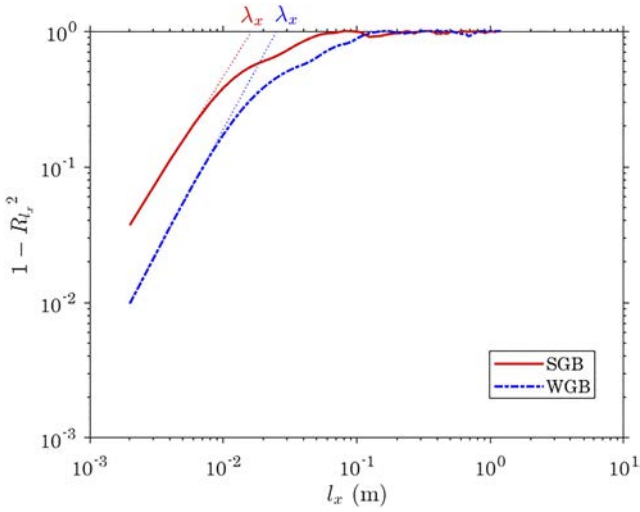


FIG. 4. Autocorrelation functions at different spacing to determine horizontal length scales for the WGB and SGB.

where l_x is the sampling length in the x direction ($= n\delta x$), $i = 1, 2, 3, \dots, n$, n is the number of points in the x direction, N is the total number of points in the x direction, and δx is the sampling interval in the x direction. In this study, we considered $\delta x = 2$ mm. The correlation length can be identified from the points with an intermediate distance l apart in which there exists a change of gradient of l in a data plot of $\log(1 - R_l^2)$ versus $\log(l)$.³⁹

It is possible to identify that the streamwise length scale λ_x for the WGB is smaller than that for the SGB, although the streamwise length scales for both the beds are larger than d_{50} . They are 2.2×10^{-2} m and 1.7×10^{-2} m for the WGB and SGB, respectively. This trend demonstrates that the bed roughness structure is more elongated in the x direction in the WGB than in the SGB.

Flow measurements for WGB and SGB were taken with $h = 0.1$ m and $U_{avg} = 0.43$ m s⁻¹ $< U_c$ ($= 0.6$ m s⁻¹). Since the threshold flow velocity was calculated to be 0.6 m s⁻¹ at $h = 0.1$ m using Neill's³⁶ formula, this indicates a clear-water condition. In the recent past,^{8,23,32} accurate estimation of the u^* was achieved by extending the RSS profiles linearly to the roughness crest as $u^* = [(-\langle u'w' \rangle)^{0.5}]_{z=z_c}$. Therefore, in this study, the u^* in the WGB and SGB were obtained from the RSS profiles to be 0.068 m s⁻¹ and 0.077 m s⁻¹, respectively. In addition, using the bed slope method [$u^* = (ghS)^{0.5}$], the u^* values in the WGB and SGB were determined to be 0.063 m s⁻¹ and 0.083 m s⁻¹, respectively. The percentage errors between two results were -7.3% and 7.8% for the WGB and SGB, respectively. Here, one can notice that the u^* in the WGB is smaller than that in the SGB, although the roughness in the former is higher than that in the latter. The reason is attributed to the lesser bed slope in the WGB than that in the SGB. The flow Reynolds number R ($= 4U_{avg}h/\nu$; where $\nu = 10^{-6}$ m² s⁻¹ at 20°C) and flow Froude number Fr [$= U_{avg}/(gh)^{0.5}$, where g is the gravitational acceleration] were determined to be 1.72×10^5 and 0.432 , respectively. The shear particle Reynolds numbers R^* ($= u^* \Delta_k/\nu$) in the WGB and SGB were calculated to be 85 and 81, respectively. In both the cases, the values of R^* were greater than 70, which confirmed that the

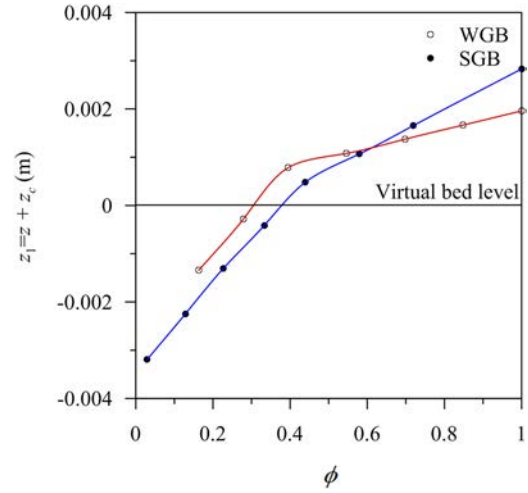


FIG. 5. Variations of roughness geometry functions ϕ in the WGB and SGB with the vertical distance z_1 ($= z + z_c$).

rough-turbulent flow prevailed. To ascertain the two-dimensionality of the flow field in the central part of the flume, flow measurements were performed at four different spanwise positions along the streamwise direction of the test section. Examination of the DA streamwise velocity and SA RSS profiles reveals that at least in the central portion of the flume (± 0.075 m off the centerline), the two-dimensionality of the flow was satisfactorily preserved.

For $z \leq 0$ (below the crest), the roughness geometry function ϕ was used as a multiplier to convert the intrinsic DA flow quantity to a superficial DA flow quantity.^{8,40-42} The distributions of the geometric function for the WGB and SGB are shown in Fig. 5.

III. RESULTS AND DISCUSSION

A. DA velocity

The contours of the dimensionless time-averaged velocities \bar{u}^+ ($= \bar{u}/u^*$, where \bar{u} is the time-averaged streamwise velocity) on a central vertical plane in the WGB and SGB are shown in Figs. 6(a) and 6(b), respectively. The horizontal and vertical axes of the contours in dimensionless form are represented as \bar{x} ($= x/L$, where L is the test section length) and \bar{z} ($= z/h$), respectively. As is traditionally observed in a hydraulically rough flow, the flow velocities in both the beds increase with the vertical distance z having streamwise spatial variations in the near-bed flow zone owing to the roughness structures. It is evident that the near-bed flow velocity in the SGB is influenced by the randomly poised roughness elements. On the other hand, the near-bed flow in the WGB is roughly stream-lined over the organized roughness structure formed by gravels with their longest axis oriented streamwise owing to water work, although the WGB roughness size is higher than the SGB roughness size.

In order to substantiate the near-bed flow heterogeneity, the instantaneous velocity vectors are plotted in Figs. 7(a) and 7(b) for the WGB and SGB, respectively. It is apparent that the near-bed velocity vectors in the WGB are less scattered than those in the SGB. In essence, two issues related to the

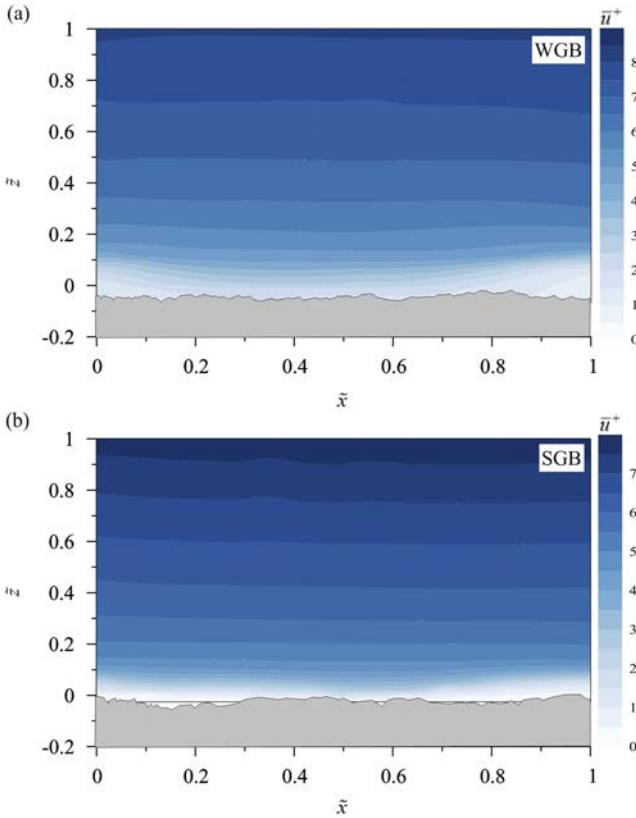


FIG. 6. Dimensionless time-averaged velocity \bar{u}^+ contours on a plane along the flume centerline in (a) the WGB and (b) the SGB.

roughness structures have now come up: the WGB organized (gravels with their longest axis oriented streamwise) and the SGB irregular (randomly poised roughness elements) bed roughness fluctuations having former with higher roughness size than latter. Then, the immediate question arises: how do the roughness structures affect the temporal and spatial velocity fluctuations that are associated with the estimates of different turbulence parameters? There is no doubt that the higher roughness size in the WGB causes to increase the temporal velocity fluctuations. Besides, the organized bed fluctuations in the WGB induce increased spatial velocity fluctuations at a quasi-regular roughness scale. Conversely, the randomly poised roughness elements in the SGB having a shorter roughness size can also induce both the temporal and spatial velocity fluctuations, but at a slightly reduced magnitude relative to the WGB case. The reason for lesser spatial velocity fluctuations in the SGB is associated with the manually screeded bed having randomly oriented gravels (note: it means that the bed roughness elements do not have organized roughness fluctuations). In Subsections III B–III F dealing with the turbulence parameters, the effects of the WGB and SGB roughness structures on temporal and spatial velocity fluctuations (in the near-bed flow zone) involved in various turbulence parameters will be clearly reflected.

To fit the data plots to a logarithmic law in the flow layer within the end of the wall shear layer and the crest, the dimensionless DA streamwise velocity $\langle u^+ \rangle = \langle \bar{u} \rangle / u_*$, where $\langle \bar{u} \rangle$ is the DA streamwise velocity) and $z^+ = [(z + \Delta z) / \Delta z]$, where Δz is the zero-plane displacement] were taken into consideration. In order to plot the experimental data, the logarithmic law is

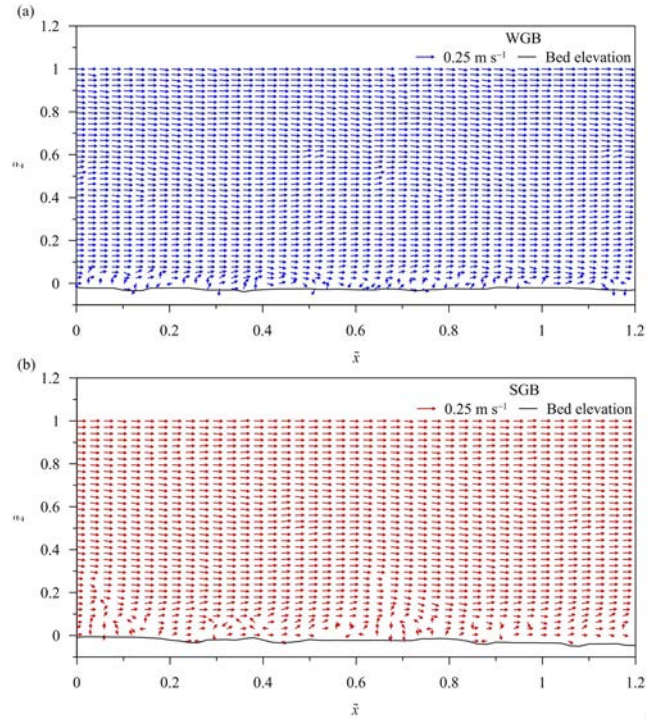


FIG. 7. Instantaneous velocity vectors at the first measuring section ($x = 6.3$ m) for (a) WGB and (b) SGB. The vector $\rightarrow 0.25 \text{ m s}^{-1}$ refers to a scale with a magnitude of $(\bar{u}^2 + \bar{w}^2)^{0.5} = 0.25 \text{ m s}^{-1}$.

expressed as

$$\langle u^+ \rangle = \frac{1}{\kappa} \ln \left(\frac{z^+}{z_0^+} \right), \quad (2)$$

where κ is the von Kármán coefficient ($= 0.41$), $z_0^+ = z_0 / \Delta z$, and z_0 is the zero-velocity level. The values of Δz and z_0 are calculated using the method proposed by Dey and Das⁸ to be 2.21×10^{-3} and 1.9×10^{-3} m, respectively, for the WGB below the crest. Likewise, the values of Δz and z_0 are 4.81×10^{-3} and 3.59×10^{-3} m, respectively, for the SGB. This indicates that the Δz and z_0 of the WGB are shallower than those of the SGB.

Figure 8 depicts that below the crest, the $\langle u^+ \rangle$ profiles in the WGB and SGB exhibit an inflection owing to the effects of the roughness geometry function. This result suggests a mixing-type flow within the interstices of gravels and a momentum sink that appears in the interfacial sublayer. Owing to interfacial flow within the gravels, the $\langle u^+ \rangle$ profiles are provoked to follow a third-order polynomial law below the crest ($z^+ \leq 1$).⁸ Importantly, the $\langle u^+ \rangle$ profiles do not follow the logarithmic law immediately above the crest. Rather they follow a linear law up to the top edge of the roughness layers ($z^+ = 4.7$ and 3.4 in the WGB and SGB, respectively) owing to the extended effect of the bed roughness and thereafter exhibit a logarithmic variation with z , as was observed by Mignot *et al.*,¹² Sarkar *et al.*,⁴⁰ and Pokrajac *et al.*⁴³ Furthermore, to understand the dispersion of the time-averaged streamwise velocity profiles \bar{u}^+ with respect to the DA streamwise velocity profile $\langle u^+ \rangle$, the standard error to the mean (SEM) analysis was performed for both the beds. The dimensionless standard error $e = [\sigma / (n u_*)]$, where σ is the standard deviation of \bar{u}^+ profiles with respect to the $\langle u^+ \rangle$ profile, and n is the number of \bar{u}^+ profiles measured

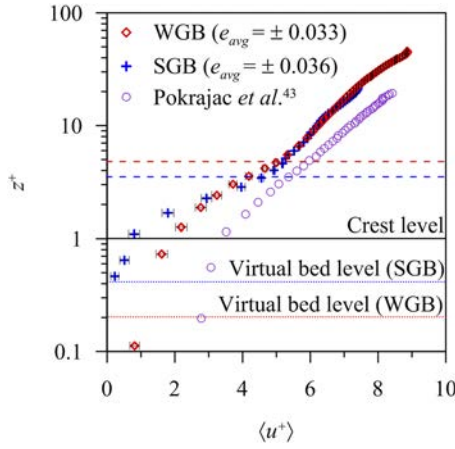


FIG. 8. Variations of the dimensionless DA streamwise velocity $\langle u^+ \rangle$ with the dimensionless vertical distance z^+ in the WGB, SGB, and Pokrajac *et al.*⁴³ Red and blue dashed lines indicate the tops of the form-induced WGB and SGB sublayers, respectively.

in the streamwise direction] was computed and shown in the form of error bars (Fig. 8). The standard average errors e_{avg} of the $\langle u^+ \rangle$ profiles in the WGB and SGB were ± 0.033 and ± 0.036 , respectively. The comparison between $\langle u^+ \rangle$ profiles in the WGB and SGB indicates that the $\langle u^+ \rangle$ in the near-bed flow zone of the former is greater than that which occurs in the latter (Fig. 8). The reason is attributed to the WGB roughness structure. Owing to the action of the water, the roughness structure had a tendency to orient the gravels to their longest axis a in the streamwise direction and intermediate axis b spanwise to them, while that in the SGB was randomly poised. This makes the near-bed flow to be relatively streamlined in the WGB than in the SGB, although the roughness in the former is higher than that in the latter. Furthermore, the $\langle u^+ \rangle$ profiles of this study are compared with those of Pokrajac *et al.*,⁴³ which attains a higher magnitude than those in the WGB and SGB. The reason is attributed to the geometrically regular roughness size in Pokrajac *et al.*⁴³ than those in the WGB and SGB.

In essence, it is apparent that after a certain distance ($z^+ \geq 3$), the $\langle u^+ \rangle$ profile in the SGB starts to increase, becoming slightly greater than that in the WGB near the free surface (Fig. 8). This implies that in the near-bed flow zone, the magnitude of $\langle u^+ \rangle$ in the WGB is greater than that in the SGB owing to differences in bed surface roughness orientation. However,

the effect of the bed roughness decreases as z^+ increases and one moves toward the free surface.

B. SA Reynolds shear stress and form-induced shear stress

For steady, uniform flow over a macro-rough bed, the spatially averaged Reynolds-averaged Navier-Stokes (RANS) equations provide a modified concept of the total fluid shear stress $\langle \bar{\tau} \rangle$.^{8,17,32,44} The $\langle \bar{\tau} \rangle$ is expressed as

$$\langle \bar{\tau} \rangle = \langle \tau_f \rangle + \langle \bar{\tau}_{uw} \rangle + \langle \bar{\tau}_v \rangle, \quad (3)$$

where $\langle \tau_f \rangle$ is the form-induced shear stress ($= -\rho \langle \tilde{u} \tilde{w} \rangle$), ρ is the mass density of fluid, \tilde{u} and \tilde{w} are the spatial velocity fluctuations in the streamwise and vertical directions, respectively, $\langle \bar{\tau}_{uw} \rangle$ is the SA RSS ($= -\rho \langle u' w' \rangle$), u' and w' are the temporal velocity fluctuations in the streamwise and vertical directions, respectively, $\langle \bar{\tau}_v \rangle$ is the DA viscous shear stress ($= \rho \nu d\langle \bar{u} \rangle / dz$), and ν is the coefficient of fluid kinematic viscosity. The $\langle \bar{\tau} \rangle$ must be balanced by gravity, and therefore it has the linear profile $\langle \bar{\tau}(\tilde{z} \geq 1) \rangle \times (\rho u_*^2)^{-1} = 1 - \tilde{z}$. The shear stresses ($\langle \bar{\tau} \rangle$, $\langle \bar{\tau}_{uw} \rangle$, $\langle \tau_f \rangle$, and $\langle \bar{\tau}_v \rangle$) are made dimensionless by multiplying by $(\rho u_*^2)^{-1}$ and represented as $\langle \bar{\tau} \rangle$, $\langle \bar{\tau}_{uw} \rangle$, $\langle \tau_f \rangle$, and $\langle \bar{\tau}_v \rangle$.

The variations of $\langle \bar{\tau}_{uw} \rangle$ with \tilde{z} in the WGB and SGB are shown in Fig. 9(a). The peak values of $\langle \bar{\tau}_{uw} \rangle$ occur at $\tilde{z} = 0.2$ and 0.27 in the WGB and SGB, respectively, and then decrease as \tilde{z} increases further. In both the beds, the $\langle \bar{\tau}_{uw} \rangle$ profiles follow the linear law (linear gravity line) with \tilde{z} after reaching their peaks. The $\langle \bar{\tau}_{uw} \rangle$ values start to decrease from $\tilde{z} = 0.15$ and 0.2 in the WGB and SGB, respectively, as \tilde{z} decreases. However, for $\tilde{z} < 0.14$, the rate of decrease of $\langle \bar{\tau}_{uw} \rangle$ becomes faster in the SGB than in the WGB. Damping of $\langle \bar{\tau}_{uw} \rangle$ in the near-bed flow zone occurs owing to decreased temporal velocity fluctuations.^{8,12,33,40,45} The results obtained in this study are compared with those in Dey and Das⁸ and Nikora *et al.*²⁴ It shows that all the $\langle \bar{\tau}_{uw} \rangle$ profiles follow a similar trend, except that of Nikora *et al.*²⁴ The $\langle \bar{\tau}_{uw} \rangle$ profiles depart from the linear gravity line and dampen within the respective form-induced and interfacial sublayers, resulting from the effects of near-bed flow heterogeneity. Furthermore, the comparison illustrates that in the near-bed flow zone, a higher roughness in the WGB induces a greater value of $\langle \bar{\tau}_{uw} \rangle$ than that in the SGB that possessed a smaller roughness. According to Nezu and Nakagawa,⁴⁶ the temporal velocity fluctuations (u' and w') are highly influenced by the bed roughness. To be explicit,

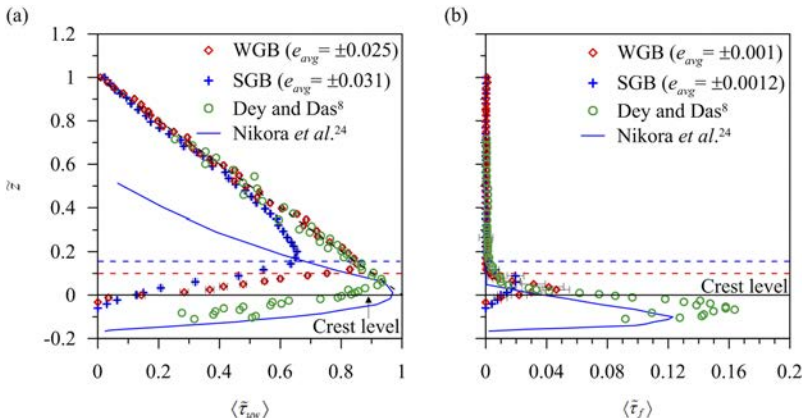


FIG. 9. Variations of the dimensionless (a) SA RSS $\langle \bar{\tau}_{uw} \rangle$ and (b) form-induced shear stress $\langle \bar{\tau}_f \rangle$ with the dimensionless vertical distance \tilde{z} in the WGB and SGB. The results obtained in this study are compared with those in Dey and Das⁸ and Nikora *et al.*²⁴

in this study, the bed roughness of the WGB is higher than that of the SGB, giving rise to higher u' and w' and resulting in greater $\langle \tilde{\tau}_{uw} \rangle$ values in the former than in the latter. This result is in conformity with the findings of Dey and Das⁸ and Nikora *et al.*²⁴ Furthermore, for the RSS profiles in both the beds, the standard errors were computed and made dimensionless by dividing u_*^2 . The average standard errors e_{avg} for the WGB and SGB were computed to be ± 0.025 and ± 0.031 , respectively.

Figure 9(b) presents the variations of $\langle \tilde{\tau}_f \rangle$ with \tilde{z} in the WGB and SGB. The $\langle \tilde{\tau}_f \rangle$ starts to develop at $\tilde{z} = 0.1$ and 0.14 in the WGB and SGB, respectively. This level, which represents the lower extremity of the wall shear layer, is considered to be the threshold of form-induced sublayer development.^{8,25} Hence, this criterion is used to determine that the thicknesses of the form-induced sublayers in the WGB and SGB are $0.1h$ and $0.14h$, respectively. Within the form-induced sublayer, the $\langle \tilde{\tau}_f \rangle$ profiles grow gradually as \tilde{z} decreases. In the WGB, the magnitude of $\langle \tilde{\tau}_f \rangle$ attains its peak close to the crest ($\tilde{z} = 0.025$), while in the SGB, the peak appears in the upper portion of the form-induced sublayer ($\tilde{z} = 0.09$). Thereafter, the values associated with both the beds start to decline as \tilde{z} decreases. The magnitudes of spatial velocity fluctuations (\tilde{u} and \tilde{w}) are responsible for this trend in $\langle \tilde{\tau}_f \rangle$. Within the form-induced sublayer, large \tilde{u} and \tilde{w} values give rise to higher $\langle \tilde{\tau}_f \rangle$ values. Below the crest ($\tilde{z} < 0$), these values are small and thus $\langle \tilde{\tau}_f \rangle$ reduces significantly.^{8,12,32,40,47} The standard errors of the $\langle \tilde{\tau}_f \rangle$ profiles in the near-bed flow zone are larger than those above the roughness layer, where they are negligible for both the beds. Like the RSS profiles, the standard errors of $\langle \tilde{\tau}_f \rangle$ profiles were computed and made dimensionless by dividing u_*^2 . The average standard errors e_{avg} are ± 0.001 and ± 0.0012 for the WGB and SGB, respectively. Furthermore, owing to the spatial variability of roughness elements over the entire test section, variations in the spatial velocity fluctuations are relatively higher than the temporal velocity fluctuations. Therefore, in this study, the error bars associated with the \tilde{u} and \tilde{w} in Fig. 9(b) are to some extent larger than those associated with the u' and w' in Fig. 9(a).

For the comparison, the $\langle \tilde{\tau}_f \rangle$ profiles of Dey and Das⁸ and Nikora *et al.*²⁴ are also shown in Fig. 9(b). The comparison corroborates that they follow similar trends, but with different magnitudes. According to Dey and Das⁸ and Sarkar *et al.*,⁴⁰ higher bed surface roughness produces large \tilde{u} and \tilde{w} values, yielding an increased magnitude of $\langle \tilde{\tau}_f \rangle$. In this study, the bed

roughness in the WGB is higher than that in the SGB, but smaller than those in Dey and Das⁸ and Nikora *et al.*²⁴ As a result, the $\langle \tilde{\tau}_f \rangle$ in the WGB attains a higher value than that in the SGB, but remains smaller than $\langle \tilde{\tau}_f \rangle$ and $\langle \tilde{\tau}_f \rangle$ in Dey and Das⁸ and Nikora *et al.*,²⁴ respectively. This indicates that in the near-bed flow zone, the flow is more heterogeneous in the WGB than in the SGB.

The variations of $\langle \tilde{\tau}_{uw} \rangle$, $\langle \tilde{\tau}_f \rangle$, $\langle \tilde{\tau}_v \rangle$, and $\langle \tilde{\tau} \rangle$ with \tilde{z} in the WGB and SGB are presented in Figs. 10(a) and 10(b). In both the beds, the $\langle \tilde{\tau}_{uw} \rangle$ profiles dominate throughout the flow depth, except in close proximity to the bed. In the near-bed flow zone ($\tilde{z} < 0.2$), the time-averaged flow becomes spatially heterogeneous, leading to a decrease in $\langle \tilde{\tau}_{uw} \rangle$, although the reduction in $\langle \tilde{\tau}_{uw} \rangle$ is compensated for by $\langle \tilde{\tau}_f \rangle$ and $\langle \tilde{\tau}_v \rangle$. As a result, the $\langle \tilde{\tau} \rangle$ profiles depart from the linear gravity profile. This is resulted from the form-induced fluctuations owing to the influence of the local flow heterogeneity. Moreover, in the near-bed zone, besides the form-induced fluctuations, a form-drag-induced stress is also prevalent.²⁴ However, little progress has so far been made to estimate the form-drag-induced stress, because its precise estimation can only be obtained from the integration of the pressure distribution across the frontal surface of the gravels.^{8,45} Hence, in this study, the $\langle \tilde{\tau} \rangle$ in both the WGB and SGB are not equaling unity near the crest. Similar observations have also been reported by previous researchers.^{8,12,32,40,41,45} In both the beds, the $\langle \tilde{\tau} \rangle$ profiles follow the linear gravity line above the wall shear layer ($\tilde{z} \geq 0.2$), as is typically observed in a zero-pressure gradient flow, approximately equaling the magnitudes of $\langle \tilde{\tau}_{uw} \rangle$, while the magnitudes of $\langle \tilde{\tau}_f \rangle$ and $\langle \tilde{\tau}_v \rangle$ are negligible. From Figs. 10(a) and 10(b), one notices that the RSS peaks appear well above the form-induced sublayer. This implies that u' and w' reach their maxima at this level owing to an intense turbulent mixing process in the near-bed flow zone. This fits with the observations of Manes *et al.*³² and Ferraro *et al.*⁴¹

Figure 11 illustrates the variations of the dimensionless form-induced shear stress to SA RSS ratio $\langle \tilde{\tau}_f \rangle / \langle \tilde{\tau}_{uw} \rangle$ with \tilde{z} in the WGB and SGB. The $\langle \tilde{\tau}_f \rangle / \langle \tilde{\tau}_{uw} \rangle$ profiles start to grow near the top of the roughness layer and then gradually increase as \tilde{z} decreases in both the beds. In the WGB, the $\langle \tilde{\tau}_f \rangle / \langle \tilde{\tau}_{uw} \rangle$ attains its peak at the crest ($\tilde{z} = 0$), while the peak appears just below the crest ($\tilde{z} = -0.025$) in the SGB. Thereafter, they both decrease rapidly with \tilde{z} . The reduction in $\langle \tilde{\tau}_f \rangle / \langle \tilde{\tau}_{uw} \rangle$ within the interfacial sublayer ($\tilde{z} < 0$) is associated with the reduction in $\langle \tilde{\tau}_f \rangle$ relative to $\langle \tilde{\tau}_{uw} \rangle$.^{8,40} Comparing the $\langle \tilde{\tau}_f \rangle / \langle \tilde{\tau}_{uw} \rangle$ profiles in

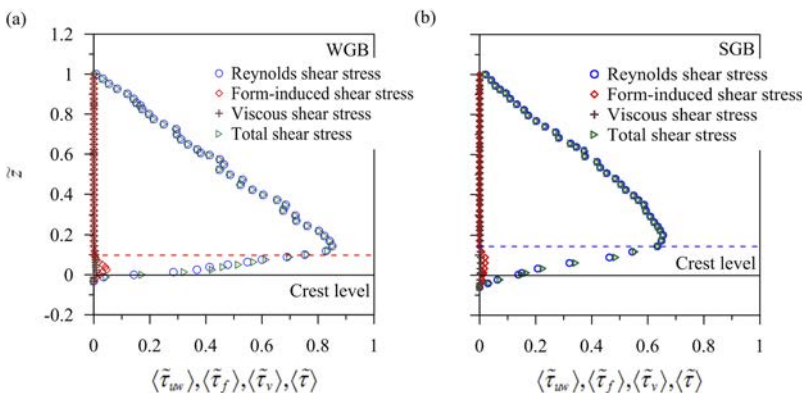


FIG. 10. Variations of the dimensionless SA RSS $\langle \tilde{\tau}_{uw} \rangle$, form-induced shear stress $\langle \tilde{\tau}_f \rangle$, DA viscous shear stress $\langle \tilde{\tau}_v \rangle$, and total shear stress $\langle \tilde{\tau} \rangle$ with the dimensionless vertical distance \tilde{z} in (a) the WGB and (b) the SGB.

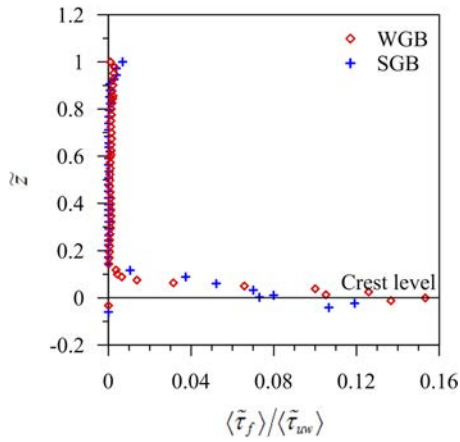


FIG. 11. Variations of the dimensionless form-induced shear stress to SA RSS ratio $\langle \tilde{\tau}_f \rangle / \langle \tilde{\tau}_{uw} \rangle$ with the dimensionless vertical distance \tilde{z} in the WGB and SGB.

the WGB and SGB, it is found that the former is greater than the latter. According to Dey and Das,⁸ the magnitude of the peak of $\langle \tilde{\tau}_f \rangle / \langle \tilde{\tau}_{uw} \rangle$ depends on the roughness size. The peak of $\langle \tilde{\tau}_f \rangle / \langle \tilde{\tau}_{uw} \rangle$ is larger at higher roughness sizes than at lower ones. In this study, the bed surface roughness of the WGB is larger than that of the SGB, producing a larger peak $\langle \tilde{\tau}_f \rangle / \langle \tilde{\tau}_{uw} \rangle$ in the former than in the latter.

C. SA Reynolds and form-induced normal stresses

The streamwise and vertical SA Reynolds normal stresses are expressed as $\langle \sigma_{uu} \rangle = \rho \langle u'u' \rangle$ and $\langle \sigma_{ww} \rangle = \rho \langle w'w' \rangle$, respectively, and made dimensionless as $(\langle \hat{\sigma}_{uu} \rangle, \langle \hat{\sigma}_{ww} \rangle) = (\langle \sigma_{uu} \rangle, \langle \sigma_{ww} \rangle) \times (\rho u_*^2)^{-1}$. The dimensionless form-induced normal stresses are expressed in a similar manner as $(\langle \hat{\sigma}_{uu} \rangle, \langle \hat{\sigma}_{ww} \rangle) = \rho (\langle \tilde{u}\tilde{u} \rangle, \langle \tilde{w}\tilde{w} \rangle) \times (\rho u_*^2)^{-1}$ in the streamwise and vertical directions, respectively. The behavior of the dimensionless SA streamwise Reynolds normal stress $\langle \hat{\sigma}_{uu} \rangle$ with respect to \tilde{z} in the WGB and SGB is shown in Fig. 12(a). In both the beds, the $\langle \hat{\sigma}_{uu} \rangle$ increases with \tilde{z} within the form-induced sublayer attaining a peak value above the crest. The peak of $\langle \hat{\sigma}_{uu} \rangle \approx 2.91$ in the WGB occurs just above the crest ($\tilde{z} = 0.025$), whereas the peak of $\langle \hat{\sigma}_{uu} \rangle \approx 1.95$ in the SGB occurs near the top of the form-induced sublayer ($\tilde{z} = 0.09$). In both the cases, the $\langle \hat{\sigma}_{uu} \rangle$ decreases with further increases in \tilde{z} . According to Dey and Das,⁸ Sarkar *et al.*,⁴⁰ and Ferraro *et al.*,⁴¹ intense fluid mixing that occurs in the presence of bed roughness is

to increase $\langle \hat{\sigma}_{uu} \rangle$ in the form-induced sublayer. However, the $\langle \hat{\sigma}_{uu} \rangle$ reduces within the interfacial sublayer owing to damping of the fluid mixing intensity.^{8,40,41}

A consistency in the trends is found when the $\langle \hat{\sigma}_{uu} \rangle$ profiles of this study are compared with those of Dey and Das⁸ and Nikora *et al.*²⁴ [Fig. 12(a)]. The $\langle \hat{\sigma}_{uu} \rangle$ profiles attain their peaks near the crest for all the cases, except that for Nikora *et al.*²⁴ The possible reason is attributed to the loosely packed gravels in Nikora *et al.*²⁴ A close examination of Fig. 12(a) suggests that the main discrepancy in these profiles lies in the magnitudes of $\langle \hat{\sigma}_{uu} \rangle$. For a given \tilde{z} , the $\langle \hat{\sigma}_{uu} \rangle$ in the WGB has a greater magnitude than that in the SGB, implying that the WGB exhibits greater u' fluctuations than the SGB. However, the magnitudes of $\langle \hat{\sigma}_{uu} \rangle$ in the WGB remain smaller than those in Dey and Das⁸ and Nikora *et al.*²⁴ owing to greater u' in the latter two cases than the former. According to Nezu and Nakagawa,⁴⁶ u' is directly associated with the bed roughness. To be precise, in this study, the higher bed roughness associated with the WGB causes its u' fluctuations to be enhanced, increasing the magnitude of $\langle \hat{\sigma}_{uu} \rangle$ in the WGB relative to that in the SGB. The $\langle \hat{\sigma}_{uu} \rangle$ profiles have average standard errors e_{avg} of ± 0.017 for the WGB and ± 0.028 for the SGB.

Figure 12(b) shows how the dimensionless SA vertical Reynolds normal stress $\langle \hat{\sigma}_{ww} \rangle$ varies with \tilde{z} in the WGB and SGB. In the WGB, the $\langle \hat{\sigma}_{ww} \rangle$ reaches its peak ($\langle \hat{\sigma}_{ww} \rangle \approx 0.58$) at $\tilde{z} = 0.37$, whereas in the SGB, the peak ($\langle \hat{\sigma}_{ww} \rangle \approx 0.75$) appears at $\tilde{z} = 0.44$. Thereafter, the magnitudes of $\langle \hat{\sigma}_{ww} \rangle$ decrease gradually as \tilde{z} increases in both the beds. This suggests that above the crest, fluid mixing is induced by bed roughness, which enhances w' fluctuations.^{8,41} However, the effects of mixing on w' within the interfacial sublayer are weaker than those above the crest resulting in a lower $\langle \hat{\sigma}_{ww} \rangle$. The $\langle \hat{\sigma}_{ww} \rangle$ profiles of Dey and Das⁸ and Nikora *et al.*²⁴ are also shown in Fig. 12(b) for the comparison with those obtained in this study. Similar to Fig. 12(a), the peak values in $\langle \hat{\sigma}_{ww} \rangle$ profiles for three cases occur above the crest, whereas for Nikora *et al.*,²⁴ it is found to be below the crest. The reason is the same as stated earlier. It is evident from Fig. 12(b) that the $\langle \hat{\sigma}_{ww} \rangle$ profile in the WGB achieves a higher magnitude than that in the SGB. It implies that the higher bed roughness associated with the WGB, relative to the SGB, induces to increase the w' fluctuations and in turn, the magnitude of $\langle \hat{\sigma}_{ww} \rangle$ is enhanced in the WGB. This phenomenon corresponds to the findings of Dey and Das,⁸ Nikora *et al.*,²⁴ and Sarkar *et al.*⁴⁰ The average standard errors e_{avg} in $\langle \hat{\sigma}_{ww} \rangle$

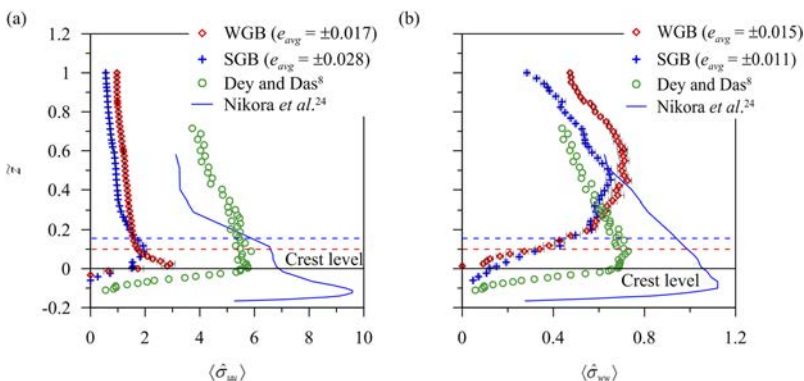


FIG. 12. Variations of the dimensionless SA (a) streamwise $\langle \hat{\sigma}_{uu} \rangle$ and (b) vertical Reynolds normal stress $\langle \hat{\sigma}_{ww} \rangle$ with dimensionless vertical distance \tilde{z} in the WGB and SGB. The results obtained in this study are compared with those in Dey and Das⁸ and Nikora *et al.*²⁴

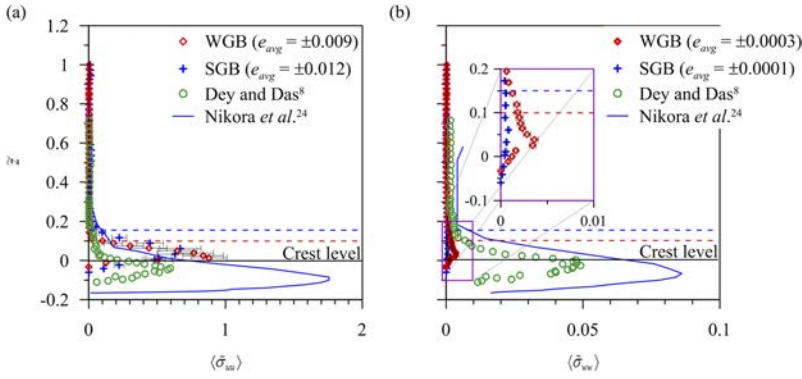


FIG. 13. Variations of the dimensionless (a) streamwise $\langle \tilde{\sigma}_{uu} \rangle$ and (b) vertical form-induced normal stress $\langle \tilde{\sigma}_{ww} \rangle$ with the dimensionless vertical distance \tilde{z} in the WGB and SGB. The results obtained in this study are compared with those in Dey and Das⁸ and Nikora *et al.*²⁴

profiles calculated for the WGB and SGB are ± 0.015 and ± 0.011 , respectively.

The behaviors of the dimensionless streamwise form-induced normal stress $\langle \tilde{\sigma}_{uu} \rangle$ in the WGB and SGB are presented in Fig. 13(a). In both the beds, the $\langle \tilde{\sigma}_{uu} \rangle$ profiles grow as \tilde{z} decreases, starting from $\tilde{z} = 0.1$ to $\tilde{z} = 0.14$, respectively. In the WGB, the peak of $\langle \tilde{\sigma}_{uu} \rangle$ exists just above the crest ($\tilde{z} = 0.01$), whereas in the SGB, the peak occurs near the middle of the form-induced sublayer ($\tilde{z} = 0.06$). However, the $\langle \tilde{\sigma}_{uu} \rangle$ decreases with a further decrease in \tilde{z} in both the beds. This suggests that within the form-induced sublayer, the $\langle \tilde{\sigma}_{uu} \rangle$ increases owing to increased spatial velocity fluctuations \tilde{u} , whereas within the interfacial sublayer, the $\langle \tilde{\sigma}_{uu} \rangle$ decreases with \tilde{u} . Above the form-induced sublayer, the $\langle \tilde{\sigma}_{uu} \rangle$ is almost negligible in both the beds. The average standard errors e_{avg} of the $\langle \tilde{\sigma}_{uu} \rangle$ profiles are of ± 0.009 and ± 0.012 for the WGB and SGB, respectively. Figure 13(a) demonstrates that the $\langle \tilde{\sigma}_{uu} \rangle$ in the WGB is greater than that in the SGB owing to the higher \tilde{u} in the former. However, the WGB $\langle \tilde{\sigma}_{uu} \rangle$ is found to be less when it is compared with that of Nikora *et al.*²⁴ This confirms that \tilde{u} are directly associated with the roughness size. The $\langle \tilde{\sigma}_{uu} \rangle$ profiles of Dey and Das⁸ are slightly smaller in magnitude than those obtained in the WGB. The roughness structure formed by the gravels in the WGB was well organized (as discussed in Sec. III A), whereas in Dey and Das,⁸ the roughness structure was randomly poised. This may result in smaller values of $\langle \tilde{\sigma}_{uu} \rangle$ in Dey and Das⁸ than those in the WGB.

Figure 13(b) shows the dimensionless vertical form-induced normal stress $\langle \tilde{\sigma}_{ww} \rangle$ variations in the WGB and SGB. Furthermore, in order to have an enlarged view, the $\langle \tilde{\sigma}_{ww} \rangle$ profiles in the near-bed flow zone are shown in the inset in Fig. 13(b). As with the $\langle \tilde{\sigma}_{uu} \rangle$ profiles, the $\langle \tilde{\sigma}_{ww} \rangle$ profiles reflect similar trends in both the beds. The $\langle \tilde{\sigma}_{ww} \rangle$ profiles in the WGB and SGB reach their peaks at $\tilde{z} = 0.025$ and 0.075 , respectively. For $\tilde{z} < 0$, the $\langle \tilde{\sigma}_{ww} \rangle$ decreases significantly with \tilde{z} . The magnitude of $\langle \tilde{\sigma}_{ww} \rangle$ depends on the variations in the spatial velocity fluctuations \tilde{w} .^{8,12,40,41,48} The comparative study suggests that the $\langle \tilde{\sigma}_{ww} \rangle$ values in both Dey and Das⁸ and Nikora *et al.*²⁴ are much larger than those obtained in this study. This occurs as a result of much higher roughness elements used in Dey and Das⁸ and Nikora *et al.*²⁴ than those in the WGB and SGB, because higher roughness induces greater \tilde{w} . Reverting to this study, Fig. 13(b) shows that there exists a difference between the peak values in the WGB and SGB. The possible reason

behind this is their difference in roughness size. In the $\langle \tilde{\sigma}_{ww} \rangle$ profiles, the average standard errors e_{avg} for the WGB and SGB are of ± 0.0003 and ± 0.0001 , respectively. One can notice that the error bars associated with $\langle \tilde{\sigma}_{uu} \rangle$ profiles are longer than those with $\langle \tilde{\sigma}_{ww} \rangle$ profiles. The reason is attributed to the spatial flow variability in the streamwise direction than that in the vertical direction.

D. DA Prandtl mixing length

The mixing length concept was introduced first by Prandtl.⁴⁹ The mixing length (l) is defined as the average length travelled by the fluid parcels from their generation to degeneration to change their momentum in the ambient fluid. To apply this concept to flow over a macro-rough bed, one must double-average the Prandtl mixing length. Thus, the DA Prandtl mixing length $\langle l \rangle$ in flow over a gravel bed can be given by

$$\langle l \rangle = \frac{(\overline{\langle u'w' \rangle})^{0.5}}{d\langle \bar{u} \rangle/dz}. \quad (4)$$

The DA Prandtl mixing length $\langle l \rangle$ is expressed in dimensionless form as $\langle \hat{l} \rangle = \langle l \rangle/k_s$. Figure 14 shows how the $\langle \hat{l} \rangle$ varies with \tilde{z} in the WGB and SGB. In the context of existing (traditional) understanding of l in a hydraulically rough flow, l varies linearly with z within the wall shear layer ($z \leq 0.2h$).²³ It is however evident that the $\langle \hat{l} \rangle$ in the WGB almost varies linearly with \tilde{z} up to $z \approx 0.2h$, complying with the traditional

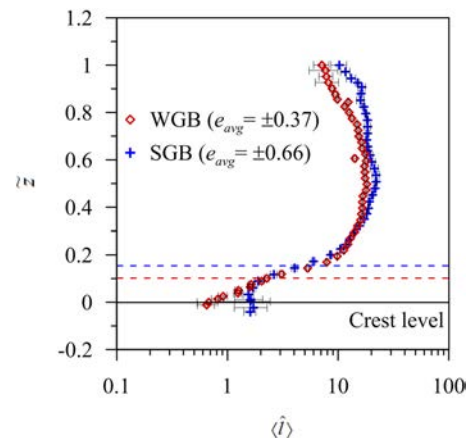


FIG. 14. Variations of the dimensionless DA Prandtl mixing length $\langle \hat{l} \rangle$ with the dimensionless vertical distance \tilde{z} in the WGB and SGB.

variation. On the other hand, in the case of the SGB, the $\langle \hat{l} \rangle$ remains almost invariant with \tilde{z} in the close proximity of the bed up to $z \approx 0.05h$; however, it varies linearly for $0.05 \geq \tilde{z} \geq 0.2$. Thereafter, the values of $\langle \hat{l} \rangle$ in both the beds grow slowly becoming almost invariant with \tilde{z} as one moves upward. The possible reason for the departure of the near-bed $\langle \hat{l} \rangle$ profile in the SGB from that in the WGB is attributed to the effects of randomly poised roughness structures in the SGB. Owing to the randomly poised roughness structures in the SGB, the flow velocity decelerates in the near-bed flow zone (as earlier discussed in Sec. III A). In addition, smaller roughness size in the SGB than that in the WGB is to produce lesser near-bed u' and w' in the SGB than those in the WGB. As a result, in the near-bed flow zone, the $\langle \hat{l} \rangle$ in the SGB is found to be smaller than that in the WGB. The average standard errors e_{avg} of the $\langle \hat{l} \rangle$ profiles vary within the range of ± 0.37 for the WGB and ± 0.66 for the SGB.

E. SA turbulent kinetic energy and form-induced turbulent kinetic energy fluxes

The SA TKE fluxes are made dimensionless as $\langle F_{ku} \rangle, \langle F_{kw} \rangle = (\langle f_{ku} \rangle, \langle f_{kw} \rangle) \times u_*^{-3}$. Variations of the dimensionless SA streamwise $\langle F_{ku} \rangle$ and vertical $\langle F_{kw} \rangle$ TKE fluxes with \tilde{z} in the WGB and SGB are shown in Figs. 15(a) and 15(b), respectively. Since the flow measurement was two-dimensional, the streamwise and vertical TKE fluxes are therefore estimated using $f_{ku} = 0.75(\overline{u'u'u'} + \overline{u'w'w'})$ and $f_{kw} = 0.75(\overline{u'u'w'} + \overline{w'w'w'})$, respectively.²³ In Fig. 15(a), the $\langle F_{ku} \rangle$ in the WGB starts positive, reaching its peak just above the crest ($\tilde{z} = 0.025$). It then decreases as \tilde{z} increases further, but remains positive until $\tilde{z} = 0.1$. The $\langle F_{ku} \rangle$ profile in the SGB follows a trend similar to that in the WGB. The positive peak of $\langle F_{ku} \rangle$ in the SGB appears at $\tilde{z} \approx 0.01$ and the sign of the $\langle F_{ku} \rangle$ changes after $\tilde{z} = 0.088$. According to Dey and Das,⁸ Mignot *et al.*,¹² and Sarkar *et al.*,⁴⁰ a positive $\langle F_{ku} \rangle$ value indicates a streamwise transport of the TKE flux, whereas a negative value suggests an upstream transport of the TKE flux. Figure 15(a) depicts that the $\langle F_{ku} \rangle$ in the WGB is greater than that in the SGB, implying the WGB to have higher u' and w' than the SGB. However, the $\langle F_{ku} \rangle$ in the WGB remain smaller than that in Mignot *et al.*¹² owing to higher u' and w' in the latter than that in the former. Moreover, the u' and w' fluctuations are directly associated with the bed roughness, as discussed

earlier. To be explicit, in this study, owing to the higher roughness in the WGB than that in the SGB, the $\langle F_{ku} \rangle$ is greater in the former than in the latter.

In Fig. 15(b), the $\langle F_{kw} \rangle$ profiles in the WGB and SGB start with small negative values within the interfacial sublayer and attain their respective negative peaks at $\tilde{z} = 0.025$ and 0. The absolute magnitude of $\langle F_{kw} \rangle$ then starts to diminish with a further increase in \tilde{z} , becoming positive for $\tilde{z} > 0.1$ and 0.088 in the WGB and SGB, respectively. Negative and positive $\langle F_{kw} \rangle$ values indicate downward and upward transport of vertical flux, respectively.^{8,23,40,45} For the comparison, the $\langle F_{kw} \rangle$ profile of Mignot *et al.*¹² is shown in Fig. 15(b). The comparative study suggests that for a given \tilde{z} , the magnitude of $\langle F_{kw} \rangle$ follows a sequence of $\langle F_{kw} \rangle$ in Mignot *et al.*¹² $>$ $\langle F_{kw} \rangle$ in the WGB $>$ $\langle F_{kw} \rangle$ in the SGB. The reason for such sequence is attributed to descending sizes of roughness, as described earlier in reference to the $\langle F_{ku} \rangle$ profiles.

According to Dey and Das,⁸ Sarkar *et al.*,⁴⁰ and Sarkar and Dey,⁴⁵ the streamwise and vertical TKE flux profiles provide information about the bursting events. The combination of a positive $\langle F_{ku} \rangle$ and a negative $\langle F_{kw} \rangle$ gives rise to sweep or Q_4 events (that is, the inrush of fluid parcels). Conversely, the combination of a negative $\langle F_{ku} \rangle$ and a positive $\langle F_{kw} \rangle$ gives rise to ejection or Q_2 events (that is, the arrival of slowly moving fluid parcels). In this study, the sweep events are dominant up to $\tilde{z} = 0.1$ and 0.088 in the WGB and SGB, respectively [Fig. 15(a)]. By contrast, the ejection events are dominant at $\tilde{z} > 0.1$ and 0.088 in the WGB and SGB, respectively [Fig. 15(b)].

The dimensionless streamwise and vertical form-induced TKE fluxes are obtained using $\langle F_{fu} \rangle, \langle F_{fw} \rangle = (\langle f_{fu} \rangle, \langle f_{fw} \rangle) \times u_*^{-3}$, respectively, where $\langle f_{fu} \rangle$ is the streamwise form-induced TKE flux expressed as $0.75(\langle \tilde{u}\tilde{u}\tilde{u} \rangle + \langle \tilde{u}\tilde{w}\tilde{w} \rangle)$ and $\langle f_{fw} \rangle$ is the vertical form-induced TKE flux expressed as $0.75(\langle \tilde{u}\tilde{u}\tilde{w} \rangle + \langle \tilde{w}\tilde{w}\tilde{w} \rangle)$. The behaviors of $\langle F_{fu} \rangle$ and $\langle F_{kw} \rangle$ with respect to \tilde{z} in the WGB and SGB are shown in Figs. 16(a) and 16(b), respectively. In both the beds, the $\langle F_{fu} \rangle$ starts with positive values within the interfacial sublayer and increases gradually with \tilde{z} . In the WGB, the $\langle F_{fu} \rangle$ reaches its positive peak above the crest ($\tilde{z} = 0.025$), whereas the peak appears at $\tilde{z} = 0.01$ in the SGB. Thereafter, both values tend to decrease with \tilde{z} . In both the beds, the $\langle F_{fu} \rangle$ nearly vanishes above the form-induced sublayer. The \tilde{u} fluctuations in the WGB are

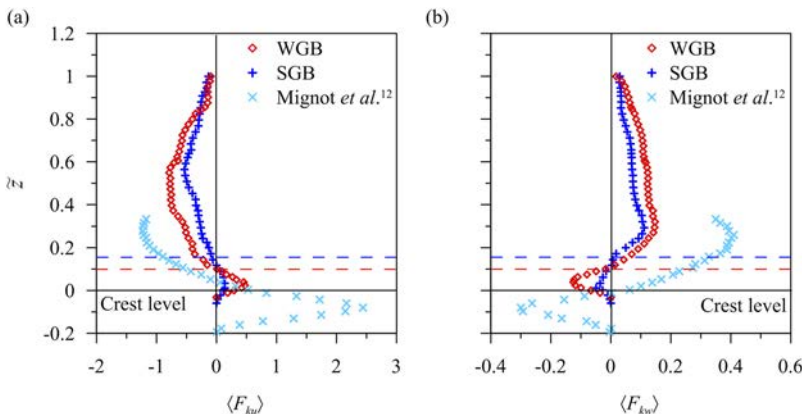


FIG. 15. Variations of the dimensionless SA (a) streamwise $\langle F_{ku} \rangle$ and (b) vertical TKE flux $\langle F_{kw} \rangle$ with the dimensionless vertical distance \tilde{z} in the WGB and SGB. The results obtained in this study are compared with those in Mignot *et al.*¹²

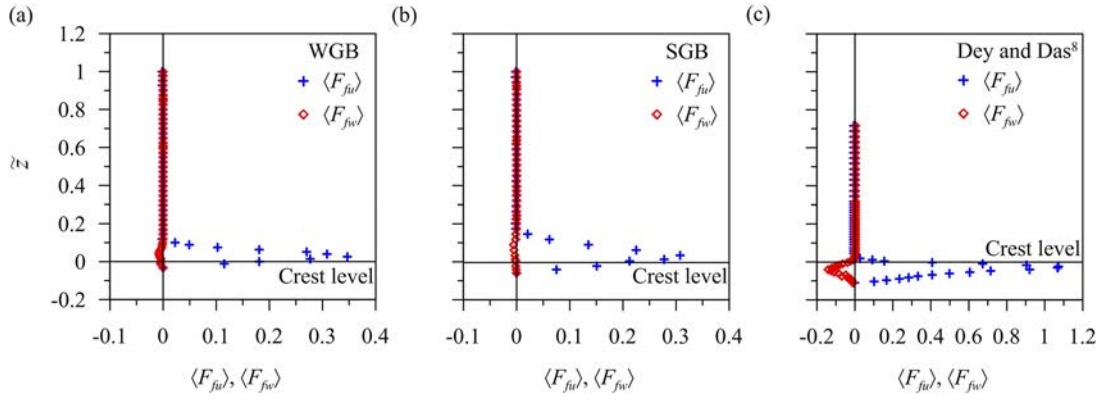


FIG. 16. Variations of the dimensionless streamwise form-induced TKE flux $\langle F_{fu} \rangle$ and the vertical form-induced TKE flux $\langle F_{fv} \rangle$ with the dimensionless vertical distance \bar{z} in (a) the WGB, (b) the SGB, and (c) Dey and Das.⁸

higher than those in the SGB, as evident from Fig. 13(a), resulting in higher $\langle F_{fu} \rangle$ in the former than in the latter at a given \bar{z} .

In both the beds, the $\langle F_{fv} \rangle$ profiles that are negative start to grow within the interfacial sublayer as \bar{z} increases [Figs. 16(a) and 16(b)]. The $\langle F_{fv} \rangle$ profiles reach their negative peaks at $\bar{z} \approx 0.039$ and 0.06 in the WGB and SGB, respectively. However, the magnitudes of $\langle F_{fv} \rangle$ gradually decrease after achieving their negative peaks as one moves toward the top edge of the form-induced sublayer and thereafter become negligible. One can argue that \tilde{w} is significantly weaker than \tilde{u} , resulting in a $\langle F_{fv} \rangle$ that is smaller than a $\langle F_{fu} \rangle$ at a given \bar{z} . Comparison of Figs. 16(a)–16(c) shows that the magnitudes of form-induced TKE fluxes in the WGB are greater than those in the SGB, whereas they remain smaller than those in Dey and Das⁸ in the near-bed flow zone. This can be interpreted as the effects of the difference in bed roughness in the three cases.

F. Conditional statistics of Reynolds shear stress

Conditional statistical analysis of the RSS provides insight into the dynamics of the coherent structure in turbulent flow.⁵⁰ In this analysis, the temporal velocity fluctuations u' and w' are decomposed into four quadrants in the $u'w'$ plane. To differentiate stronger and weaker events, the hole size H and the detection function $\lambda_{i,H}(t)$ are used. The detection function

$\lambda_{i,H}(t) = 1$ when $|u'w'| \geq H(\overline{u'u'})^{0.5}(\overline{w'w'})^{0.5}$. Otherwise $\lambda_{i,H}(t) = 0$. Hence, larger velocity fluctuations (stronger events) that contribute to the RSS can be identified from each quadrant plot by leaving the smaller velocity fluctuations (weaker events) within the hole.^{8,25,26} The contributions of bursting events to the total RSS from quadrant i outside the hole can be obtained from

$$\overline{u'w'}_{i,H} = \lim_{T \rightarrow \infty} \frac{1}{T} \int_0^T u'(t)w'(t)\lambda_{i,H}(z, t)dt, \quad (5)$$

where T is the sampling time. Depending on the sign convention, the bursting events are characterized. This includes Q_1 events, which are outward interactions ($i = 1, u' > 0$ and $w' > 0$), Q_2 events, which are ejections ($i = 2, u' < 0$ and $w' > 0$), Q_3 events, which are inward interactions ($i = 3, u' < 0$, and $w' < 0$), and Q_4 events, which are sweeps ($i = 4, u' > 0$, and $w' < 0$). The fractional contribution of the conditional RSS ($S_{i,H}$) of each event to the total RSS is represented using

$$S_{i,H} = \frac{\overline{u'w'}_{i,H}}{\overline{u'w'}}. \quad (6)$$

The variations of the DA fractional contributions $\langle S_{i,H} \rangle$ with \bar{z} in the WGB and SGB when $H = 0$ are presented in Figs. 17(a) and 17(b), respectively. Although u' and w' have small magnitudes within the interfacial sublayer, they play vital roles in the analysis of turbulence characteristics.

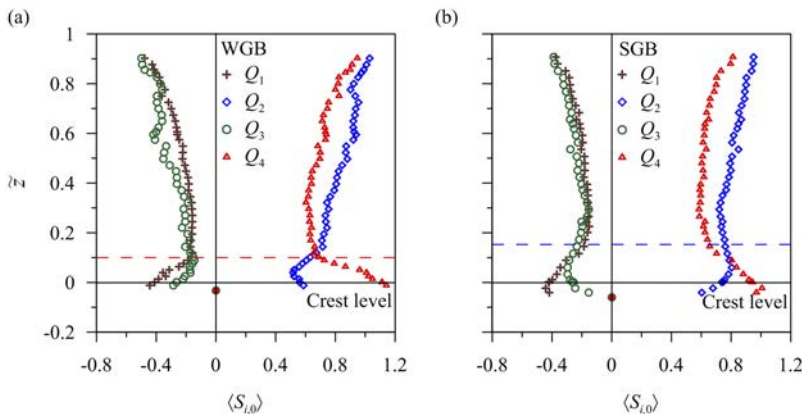


FIG. 17. Variations of the fractional contributions to the conditional SA RSS $\langle S_{i,0} \rangle$ with the dimensionless vertical distance \bar{z} in (a) the WGB and (b) the SGB.

Therefore, all plots of u' and w' at $H = 0$ are considered when calculating $\langle S_{i,H} \rangle$.^{8,45}

Figures 17(a) and 17(b) indicate that contributions from the Q_2 events to the total RSS increase with \bar{z} above the wall shear layer ($\bar{z} > 0.2$) and continue to be larger than the contributions from Q_4 events up to the free surfaces of both the beds. Contributions from Q_1 and Q_3 events are insignificant when compared to those from Q_2 and Q_4 events, as has been commonly observed in rough-bed flows.^{8,12,40,45} In Fig. 17(a), at the crest ($\bar{z} = 0$), the contributions from the Q_2 and Q_4 events represent approximately 58% and 110% ($\langle S_{2,0} \rangle \approx 0.58$ and $\langle S_{4,0} \rangle \approx 1.1$), respectively. Conversely, the contributions from Q_1 and Q_3 events at the crest are approximately 22% and 40% ($\langle S_{1,0} \rangle \approx 0.22$ and $\langle S_{3,0} \rangle \approx 0.4$), respectively. When $\bar{z} > 0$, the contribution from Q_4 events decreases as \bar{z} increases, while that from Q_2 events increases. The two contributions become equal ($\langle S_{2,0} \rangle \approx \langle S_{4,0} \rangle \approx 0.79$) at $\bar{z} = 0.1$. As \bar{z} increases further, the contribution from Q_2 events becomes larger than that from Q_4 events, becoming dominant for the rest of the vertical distance z . This indicates that sweep or Q_4 events dominate within the roughness layer ($\bar{z} = 0.1$). The dominance of sweep events indicates an inrush of faster-moving fluid parcels within the interfaces of gravels. Hence, sweep events are governed by the flow within the near-bed flow zone and consequently, the magnitude of SA RSS is diminished in this flow zone.

In the SGB, the profiles of the Q_1 , Q_2 , Q_3 , and Q_4 events follow the trends similar to those in the WGB [Fig. 17(b)]. The contribution from Q_4 events equals to that from Q_2 events ($\langle S_{2,0} \rangle \approx \langle S_{4,0} \rangle \approx 0.8$) at the middle of the form-induced sublayer ($\bar{z} = 0.088$). When $\bar{z} > 0.088$, the contribution from Q_2 events is greater than that from Q_4 events. From Figs. 17(a) and 17(b), one can see that the profiles of the Q_2 and Q_4 events in the WGB and SGB are similar, except in the near-bed flow zone. In the WGB, the contribution from Q_4 events reaches its peak at $\bar{z} = -0.025$ and then begins to decrease as

\bar{z} increases further. Within the interfacial sublayer, the contribution from the Q_4 events in the SGB increases with \bar{z} until it reaches its peak just below the crest, at which point it decreases. The contribution from Q_2 events in the WGB decreases until $\bar{z} = 0.05$, but increases with \bar{z} thereafter. By contrast, the contribution from Q_2 events in the SGB starts to increase within the interfacial sublayer, maintaining almost the same magnitude throughout the flow depth. In the near-bed flow zone, the fractional contribution to the total RSS from Q_4 events is higher in the WGB than in the SGB. One possible reason is the presence of higher u' and w' fluctuations in the WGB than in the SGB.

A quadrant analysis of the spatial velocity fluctuations, \tilde{u} and \tilde{w} , in the $\tilde{u}\tilde{w}$ domain was performed for the WGB and SGB.^{40,45} In the quadrant plots, \tilde{u} and \tilde{w} are made dimensionless by dividing by u_* . The results for the WGB and SGB are shown in Figs. 18 and 19, respectively. The \tilde{u} and \tilde{w} plots of six different vertical locations are presented at $z = -0.0025$ m (below the crest), 0 m (at the crest), 0.0025 m, 0.005 m, 0.02 m, and 0.05 m (above the crest). In the WGB, the $z = 0.005$ m, 0.0025 m, 0, and -0.0025 m plots form a pseudo-elliptical shape with the major axis inclined toward the x axis. However, for $z = 0.02$ and 0.05 m, the plots form an irregular elliptical cluster. From Fig. 18, it is apparent that \tilde{u} and \tilde{w} tend to vanish at the outer extremity and above the wall shear layer ($\bar{z} \geq 0.2$). However, these values are finite in the near-bed flow zone. The ellipse is largest at $\bar{z} = 0.025$. This indicates that the form-induced stress is at its maximum when $\bar{z} = 0.025$, decreasing when \bar{z} either increases or decreases. A similar trend is observed in the SGB (Fig. 19). Upon comparing Figs. 18 and 19, one finds that the \tilde{u} and \tilde{w} in the WGB appear to be more scattered and have higher magnitudes than those in the SGB. This implies that water work causes significant changes in gravel orientation, as well as in the bed surface roughness, resulting in higher spatial velocity fluctuations in the WGB than in the SGB.

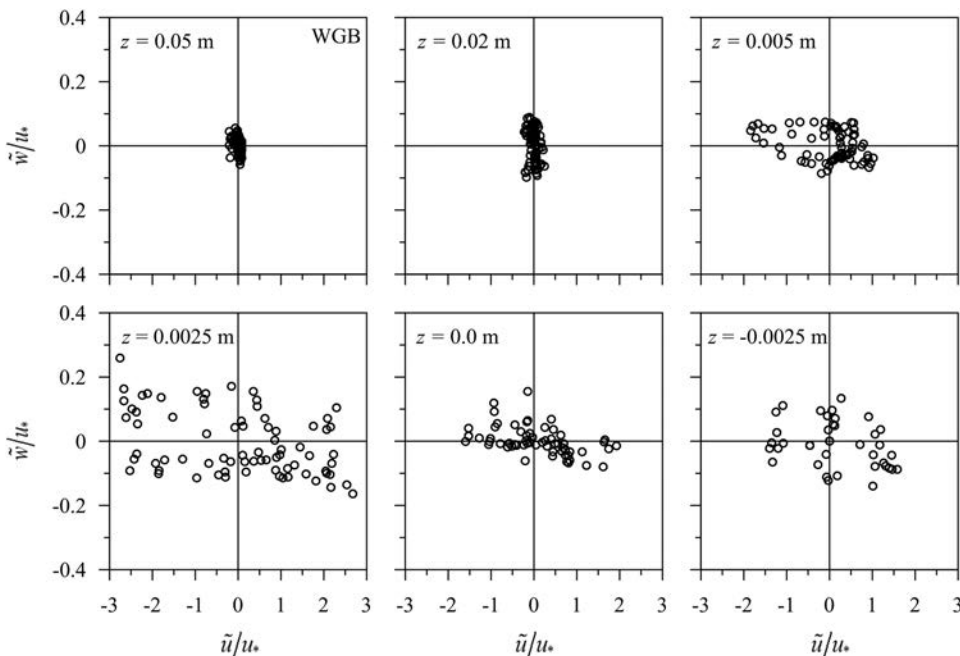


FIG. 18. Quadrant plots of spatial velocity fluctuations at different vertical distances z in the WGB.

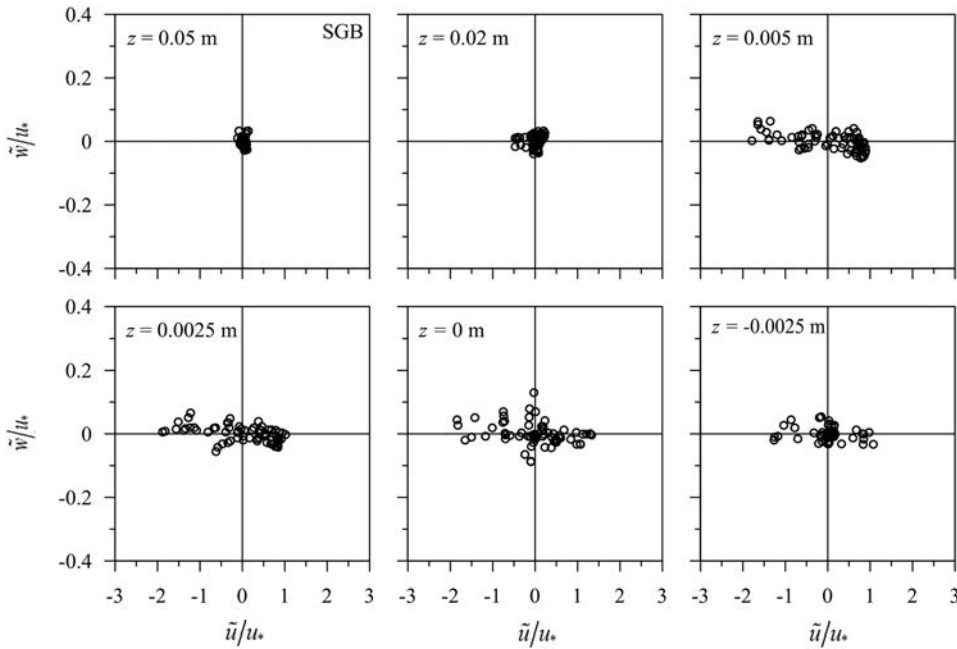


FIG. 19. Quadrant plots of spatial velocity fluctuations at different vertical distances z in the SGB.

IV. CONCLUDING REMARKS

The turbulence characteristics of flows over a WGB and an SGB were measured using a two-dimensional particle image velocimetry and analyzed by applying the DAM. Although the flow conditions in both the beds were identical, significant differences in the velocity and turbulence characteristics were noted, especially in the near-bed flow zone. This was induced by the differences between the WGB and SGB roughness structures that were composed of different orientations of surface gravels. Importantly, owing to the action of water work, the longest axis of the gravels of WGBs was oriented streamwise, and that of SGBs was randomly poised. The DA streamwise velocity profiles in both the beds follow the logarithmic law above the form-induced sublayer, but follow linear and third-order polynomial laws within the form-induced and interfacial sublayers, respectively. Although the DA streamwise velocity profiles follow a similar trend in the WGB and SGB, the near-bed velocity profile in the former is greater than that in the latter. It is resulted from the near-bed flow to be relatively streamlined in the WGB (in which the longest axis of gravels was systematically oriented streamwise) than in the SGB (in which the gravels were randomly poised), although the roughness in the former is higher than that in the latter.

In both the beds, the SA RSS profiles reach their peaks above the wall shear layer, continuing to decrease toward the free surface and closely following the linear law (linear gravity line) with vertical distance. In the near-bed flow zone, the SA RSS is larger in the WGB than in the SGB owing to the presence of larger temporal velocity fluctuations in the former. Within the roughness layer, the form-induced shear stress values in both the beds reach their peaks above the crest and thereafter decrease toward the outer edge of the form-induced sublayer. Owing to greater spatial velocity fluctuations in the WGB, the form-induced shear stress in the WGB is greater than that in the SGB. The SA Reynolds

normal stress components are small in the near-bed flow zone and grow as the vertical distance increases in both the WGB and SGB. They reach their peaks above the crest. As a result of higher temporal velocity fluctuations in the WGB, its SA Reynolds normal stress components are larger than those in the SGB.

Analysis shows that the DA Prandtl mixing lengths in the WGB and SGB are small within the interfacial sublayer. However, they increase above the form-induced sublayer. The SA TKE fluxes in the WGB are small in the near-bed flow zone and change their signs above the crest. Although similar trends appear in the SGB, significant differences between the magnitudes of the SA TKE fluxes in the WGB and SGB are observed in the near-bed flow zone.

A quadrant analysis of temporal velocity fluctuations confirms that sweep events dominate in the near-bed flow zone and that the character of this dominance changes above the crests of both the beds. Sweep events tend to dominate more in the WGB than in the SGB. This implies that the fluid in the near-bed flow zone of the WGB accelerates more than that of the SGB owing to an inrush of fluid parcels, resulting in a larger DA streamwise velocity. The spatial velocity fluctuations in both the beds were plotted. In the near-bed flow zone, the plotted clusters formed pseudo-elliptical shapes. The clusters became small beyond the roughness layer, indicating the disappearance of spatial velocity fluctuations. The quadrant plots of spatial velocity fluctuations in the WGB were more scattered than those in the SGB, indicating the influence of differences between the roughness sizes of the two beds.

In this context, it is important to mention that the above results were obtained from the flow measurements along the centerline of the flume. It is however acknowledged that the spanwise roughness could afflict the DA flow results, if the streamwise roughness distributions at spanwise locations (off the centerline) were different from those at the centerline of the

flume, but this was not the case for the beds studied, which was confirmed from the bed scanner results. In fact, the streamwise roughness distributions at spanwise locations were approximately similar to those at the centerline of the flume in both the beds.

In essence, the DAM experimental results allow us to clearly understand the impact of gravel-bed roughness in WGBs and SGBs on the turbulent flow characteristics. This study reveals that SGBs underestimate the turbulence parameters as compared to WGBs. Furthermore, the WGB preserves similar surface roughness organization and properties that are observed in a natural gravel-bed river. To be explicit, (a) the vertical length scale of the roughness elements in a WGB is less than half of the horizontal length scale of the roughness elements, (b) the gravels in the WGB have a tendency to orient their longest axis in the streamwise direction, inducing the near-bed flow to be relatively streamlined than that in the SGB, and (c) the higher spatial turbulent stresses in the WGB than those in the SGB indicate that the favorable particle orientation and direction of imbrication in the subsurface is to reduce the bulk porosity of the WGB. This scenario closely resembles to the natural gravel-bed rivers. Thus, it can be concluded that in the laboratory, the WGB is able to simulate, in a simplified manner, both the surface and subsurface properties of a natural gravel-bed river. Hence, future experiments should be performed using WGBs, as these are more representative of actual riverbed conditions. This would aid to produce more accurate estimates of near-bed turbulence parameters. By contrast, near-bed turbulence parameters obtained from experimental studies that use SGBs should be handled with care.

- ¹A. J. Grass, "Structural features of turbulent flow over smooth and rough boundaries," *J. Fluid Mech.* **50**, 233–255 (1971).
- ²B. Kironoto and W. H. Graf, "Turbulence characteristics in rough uniform open-channel flow," *Proc. Inst. Civ. Eng.: Water Maritime and Energy* **106**, 333–344 (1994).
- ³L. A. Giménez-Curto and M. A. Corniero, "Oscillating turbulent flow over very rough surfaces," *J. Geophys. Res.: Oceans* **101**, 20745–20758, <https://doi.org/10.1029/96jc01824> (1996).
- ⁴A. Dittrich and K. Koll, "Velocity field and resistance of flow over rough surface with large and small relative submergence," *Int. J. Sediment Res.* **12**, 21–33 (1997).
- ⁵V. Nikora and G. M. Smart, "Turbulence characteristics of New Zealand gravel-bed rivers," *J. Hydraul. Eng.* **123**, 764–773 (1997).
- ⁶V. Nikora and D. Goring, "Flow turbulence over fixed and weakly mobile gravel beds," *J. Hydraul. Eng.* **126**, 679–690 (2000).
- ⁷S. Dey and R. V. Raikar, "Characteristics of loose rough boundary streams at near-threshold," *J. Hydraul. Eng.* **133**, 288–304 (2007).
- ⁸S. Dey and R. Das, "Gravel-bed hydrodynamics: Double-averaging approach," *J. Hydraul. Eng.* **138**, 707–725 (2012).
- ⁹M. J. Franca and U. Lemmin, "Turbulence measurements in shallow flows in gravel-bed rivers," in *Proceedings of 7th International Conference Hydro-Science and Engineering*, Philadelphia, USA, 2006.
- ¹⁰J. F. Rodríguez and M. H. García, "Laboratory measurements of 3-D flow patterns and turbulence in straight open channel with rough bed," *J. Hydraul. Res.* **46**, 454–465 (2008).
- ¹¹V. Nikora and P. M. Rowinski, "Rough-bed flows in geophysical, environmental and engineering systems: Double averaging approach and its applications," *Acta Geophys.* **56**, 529–934 (2008).
- ¹²E. Mignot, E. Barthelemy, and D. Hurther, "Double-averaging analysis and local flow characterization of near-bed turbulence in gravel-bed channel flows," *J. Fluid Mech.* **618**, 279–303 (2009).
- ¹³E. Mignot, D. Hurther, and E. Barthelemy, "On the structure of shear stress and turbulent kinetic energy flux across the roughness layer of a gravel-bed channel flow," *J. Fluid Mech.* **638**, 423–452 (2009).
- ¹⁴J. R. Cooper and S. J. Tait, "The spatial organization of time-averaged streamwise velocity and its correlation with the surface topography of water-worked gravel beds," *Acta Geophys.* **56**, 614–641 (2008).
- ¹⁵R. J. Hardy, J. L. Best, S. N. Lane, and P. E. Carbonneau, "Coherent flow structures in a depth-limited flow over a gravel surface: The role of near-bed turbulence and influence of Reynolds number," *J. Geophys. Res.* **114**, F01003, <https://doi.org/10.1029/2007jf000970> (2009).
- ¹⁶J. R. Cooper and S. J. Tait, "Water-worked gravel beds in laboratory flumes—A natural analogue?," *Earth Surf. Processes Landforms* **34**, 384–397 (2009).
- ¹⁷K. Koll, S. J. Tait, J. Aberle, J. R. Cooper, S. J. McLelland, B. J. Murphy, and G. Massaro, "Estimating flow turbulence characteristics over water-worked gravel beds using LDA and PIV measurement systems," in *Proceedings of International Conference on Fluvial Hydraulics, River Flow, Izmir, Turkey* (Kubaba Congress Department and Travel Services, Ankara, 2008), Vol. 1, pp. 739–746.
- ¹⁸K. Koll, J. R. Cooper, J. Aberle, S. J. Tait, and A. Marion, "Investigation into the physical relationship between water-worked gravel bed armours and turbulent in-channel flow patterns," in *Proceedings of the HYDRALAB III Joint User Meeting*, Hannover, Germany, 2010.
- ¹⁹J. R. Cooper and S. J. Tait, "Spatially representative velocity measurement over water-worked gravel beds," *Water Resour. Res.* **46**, W11559, <https://doi.org/10.1029/2009wr008465> (2010).
- ²⁰J. R. Cooper and S. J. Tait, "Spatial variability in turbulent flows over water-worked gravel beds," in *Proceedings of International Conference on Fluvial Hydraulics, River Flow, Braunschweig, Germany* (Bundesanstalt für Wasserbau, Karlsruhe, 2010), Vol. 1, pp. 51–58.
- ²¹J. R. Cooper, J. Aberle, K. Koll, and S. J. Tait, "Influence of relative submergence on spatial variance and form-induced stress of gravel-bed flows," *Water Resour. Res.* **49**, 5765–5777, <https://doi.org/10.1002/wrcr.20464> (2013).
- ²²S. J. McLelland, "Coherent secondary flows over a water-worked rough bed in a straight channel," in *Coherent Flow Structures at Earth's Surface*, edited by J. G. Venditti, J. L. Best, M. Church, and R. J. Hardy (John Wiley & Sons, Chichester, UK, 2013).
- ²³S. Dey, *Fluvial Hydrodynamics: Hydrodynamic and Sediment Transport Phenomena* (Springer-Verlag, Berlin, Germany, 2014).
- ²⁴V. Nikora, D. Goring, I. McEwan, and G. Griffiths, "Spatially averaged open-channel flow over rough bed," *J. Hydraul. Eng.* **127**, 123–133 (2001).
- ²⁵V. Nikora, K. Koll, I. McEwan, S. McLean, and A. Dittrich, "Velocity distribution in the roughness layer of rough-bed flows," *J. Hydraul. Eng.* **130**, 1036–1042 (2004).
- ²⁶V. Nikora, S. McLean, S. Coleman, D. Pokrajac, I. McEwan, L. Campbell, J. Aberle, D. Clunie, and K. Koll, "Double-averaging concept for rough-bed open-channel and overland flows: Applications," *J. Hydraul. Eng.* **133**, 884–895 (2007).
- ²⁷V. Nikora, I. McEwan, S. McLean, S. Coleman, D. Pokrajac, and R. Walters, "Double-averaging concept for rough-bed open-channel and overland flows: Theoretical background," *J. Hydraul. Eng.* **133**, 873–883 (2007).
- ²⁸A. S. Monin and A. M. Yaglom, *Statistical Fluid Mechanics: Mechanics of Turbulence* (MIT Press, Cambridge, 1971), Vol. I.
- ²⁹R. M. L. Ferreira, "Turbulent flow hydrodynamics and sediment transport: Laboratory research with LDA and PIV," in *Experimental Methods in Hydraulic Research*, edited by P. Rowinski (Springer, Berlin, Heidelberg, 2011), Vol. I, pp. 67–111.
- ³⁰A. Melling, "Tracer particles and seeding for particle image velocimetry," *Meas. Sci. Technol.* **8**, 1406–1416 (1997).
- ³¹M. Raffel, C. E. Willert, S. T. Wereley, and J. Kompenhans, *Particle Image Velocimetry: A Practical Guide* (Springer-Verlag, Berlin, Germany, 2007).
- ³²C. Manes, D. Pokrajac, and I. McEwan, "Double-averaged open-channel flows with small relative submergence," *J. Hydraul. Eng.* **133**, 896–904 (2007).
- ³³C. Manes, D. Pokrajac, I. McEwan, and V. Nikora, "Turbulence structure of open channel flows over permeable and impermeable beds: A comparative study," *Phys. Fluids* **21**, 125109 (2009).
- ³⁴T. Buffin-Bélanger and A. Roy, "1 min in the life of a river: Selecting the optimal record length for the measurement of turbulence in fluvial boundary layers," *Geomorphology* **68**, 77–94 (2005).
- ³⁵M. Detert, V. Nikora, and G. H. Jirka, "Synoptic velocity and pressure fields at the water-sediment interface of streambeds," *J. Fluid Mech.* **660**, 55–86 (2010).
- ³⁶C. R. Neill, "Mean-velocity criterion for scour of coarse uniform bed material," in *Proceedings of International Association of Hydraulic Research 12th Congress*, Fort Collins, Colorado, USA, 1967, Vol. 3, pp. 46–54.

- ³⁷V. I. Nikora, D. G. Goring, and B. J. Biggs, "On gravel-bed roughness characterization," *Water Resour. Res.* **34**, 517–527, <https://doi.org/10.1029/97wr02886> (1998).
- ³⁸J. Aberle and G. M. Smart, "The influence of roughness structure on flow resistance on steep slopes," *J. Hydraul. Res.* **41**, 259–269 (2003).
- ³⁹G. M. Smart, M. J. Duncan, and J. M. Walsh, "Relatively rough flow resistance equations," *J. Hydraul. Eng.* **128**, 568–578 (2002).
- ⁴⁰S. Sarkar, A. N. Papanicolaou, and S. Dey, "Turbulence in a gravel-bed stream with an array of large gravel obstacles," *J. Hydraul. Eng.* **142**, 04016052 (2016).
- ⁴¹D. Ferraro, S. Servidio, V. Carbone, S. Dey, and R. Gaudio, "Turbulence laws in natural bed flows," *J. Fluid Mech.* **798**, 540–571 (2016).
- ⁴²J. Aberle, "Measurements of armour layer roughness geometry function and porosity," *Acta Geophys.* **55**, 23–32 (2007).
- ⁴³D. Pokrajac, I. McEwan, and V. Nikora, "Spatially averaged turbulent stress and its partitioning," *Exp. Fluids* **45**, 73–83 (2008).
- ⁴⁴L. A. Giménez-Curto and M. A. Corniero, "Flow characteristics in the interfacial shear layer between a fluid and a granular bed," *J. Geophys. Res.* **107**, 1–12, <https://doi.org/10.1029/2000jc000729> (2002).
- ⁴⁵S. Sarkar and S. Dey, "Double-averaging turbulence characteristics in flows over a gravel bed," *J. Hydraul. Res.* **48**, 801–809 (2010).
- ⁴⁶I. Nezu and H. Nakagawa, *Turbulence in Open-Channel Flows* (International Association of Hydraulic Engineering and Research Monograph, Rotterdam, The Netherlands, 1993).
- ⁴⁷J. Aberle, K. Koll, and A. Dittrich, "Form induced stresses over rough gravel-beds," *Acta Geophys.* **56**, 584–600 (2008).
- ⁴⁸J. Yuan and U. Piomelli, "Roughness effects on the Reynolds stress budgets in near-wall turbulence," *J. Fluid Mech.* **760**, R1 (2014).
- ⁴⁹L. Prandtl, "Bericht über untersuchungen zur ausgebildeten turbulenz," *Z. Angew. Math. Mech.* **5**, 136–139 (1925).
- ⁵⁰S. S. Lu and W. W. Willmarth, "Measurements of the structures of the Reynolds stress in a turbulent boundary layer," *J. Fluid Mech.* **60**, 481–511 (1973).